

# Manifestations of Local Supersolidity of $^4\text{He}$ around a Charged Molecular Impurity

Fabien Brieuc,<sup>1,2,\*</sup> Christoph Schran,<sup>1,3,†</sup> and Dominik Marx<sup>1,‡</sup>

<sup>1</sup>*Lehrstuhl für Theoretische Chemie, Ruhr-Universität Bochum, 44780 Bochum, Germany*

<sup>2</sup>*Present address: Laboratoire Matière en Conditions Extrêmes, Université Paris-Saclay, CEA, 91680 Bruyères-le-Châtel; CEA, DAM, DIF, F-91297 Arpajon, France*

<sup>3</sup>*Present address: Yusuf Hamied Department of Chemistry, University of Cambridge, Lensfield Road, Cambridge CB2 1EW, UK*

(Dated: August 15, 2023)

A frozen, solid helium core, dubbed snowball, is typically observed around cations in liquid helium. Here we discover, using path integral simulations, that around a cationic molecular impurity, protonated methane, the  $^4\text{He}$  atoms are indeed strongly localized akin to snowballs but still participate in vivid bosonic exchange induced by the ro-vibrational motion of the impurity. Such combination of solid-like order with pronounced superfluid response in the first helium shell indicates that manifestations of local supersolid behavior of  $^4\text{He}$  can be induced by charged molecules.

## INTRODUCTION

Since the ground-breaking discovery of superfluidity in liquid  $^4\text{He}$ , generations of scientists have raised the question whether such superfluid response can persist in the solid phase, i.e. *Can a Solid Be “Superfluid”?* [1]. Such a counter intuitive state, combining solid-like order with a finite superfluid fraction [2], has been theoretically proposed as early as 1969 [3, 4]. More recently, it has been suggested experimentally that supersolid states can appear in model systems, such as Bose-Einstein condensates of atomic gases at ultralow temperatures [5–7]. Computationally, evidence of a supersolid phase has been reported for atomic deuterium – yet at ultrahigh pressure conditions [8]. When it comes to finite systems substantial understanding was provided by theoretical work leading to novel experiments. In fact, pioneering path integral simulations have revealed that small para- $\text{H}_2$  clusters of specific size can exhibit spatial localization of these bosonic species at sufficiently low temperatures, reminiscent of a solid, combined with some remaining bosonic exchange [9, 10], thus suggesting supersolid behavior. But different from para- $\text{H}_2$ , such phenomena cannot appear in pure  $^4\text{He}$  clusters since they remain liquid even in the ground state given that the very weak  $\text{He} \cdots \text{He}$  interactions are a factor of 3 smaller. Overall, the existence of supersolid properties in the specific case of  $^4\text{He}$ -systems, both extended and finite, remains controversial [2, 11–14].

Here, we answer the question whether *manifestations of supersolid behavior* of  $^4\text{He}$  can be found *locally* in the first shell around charged molecular impurities in finite  $^4\text{He}$ -systems — a situation that would potentially enable experimental verification akin to discovering “*microscopic manifestation of superfluidity*” around neutral dopant molecules [15–17].

Indeed, such impurities in liquid helium have been shown to be powerful probes of “*manifestations of superfluid behavior*”, a concept introduced by seminal theory work [18], and validated experimentally a

decade later [15–17]. Charged impurities usually interact strongly with helium, creating a frozen, solid-like core around the impurity, referred to as a snowball [19]. This snowball effect has been extensively studied both theoretically [20–22] and experimentally [23–25] in the case of atomic cationic impurities, and has been linked to a local *disappearance of superfluidity* within the frozen  $^4\text{He}$  atoms of the snowball due to their strong spatial localization [20, 22, 26].

Molecular impurities have also been immersed particularly in helium nanodroplets and smaller  $^4\text{He}$  clusters [17]. Their rotational excitations have been used to probe the local microscopic superfluid response showing that “*manifestations of superfluid behavior*” can indeed be found in finite systems as small as about ten  $^4\text{He}$  atoms only [27–29]. In addition, quantum simulations have been pivotal in elucidating the impact of neutral molecular impurities on the helium environment [30–34]. Their impact is usually smaller than ions due to weaker interactions with the solvent. However, around some of the most strongly interacting neutral molecules, such as  $\text{SF}_6$ , the first solvation shell is composed of more localized  $^4\text{He}$  atoms which is linked to a *reduction* of the superfluid fraction in a way that is reminiscent of the snowball effect around ions [30, 35]. Yet, it has been shown that rigid-body rotation can lead to a non-negligible *enhancement* of the superfluid response in the first shell [36–39]. Pioneering work on the superfluid response of  $^4\text{He}$  around  $\text{C}_{20}$  has even hinted at something like nanoscale supersolidity but, akin to para- $\text{H}_2$  clusters, only for specific (“magic”) helium numbers between 28 and 31 atoms, whereas the phenomenon quickly vanishes when adding more  $^4\text{He}$  atoms [40]. Similar effects have also been seen around the completion of the second layer of helium adsorbed on graphite [41–43].

In that long-standing quest of finding manifestations of supersolid behavior in  $^4\text{He}$ , this leads to the question whether fast rotation of a strongly interacting molecular impurities could induce a pronounced superfluid response in a frozen, solid-like helium shell and, thus, could be

used as seeds for supersolid behavior in the bulk.

To answer this fundamental question, we set out to study helium solvation of an ionic molecular impurity, protonated methane, using quantum simulations. Why  $\text{CH}_5^+$ ? Firstly, its interaction with  $^4\text{He}$  is about four times stronger than other strongly interacting neutral species. Secondly,  $\text{CH}_5^+$  is a prototype of the class of so-called fluxional molecules, being subject to large-amplitude motion leading to a full delocalization of its hydrogens due to pseudo-rotational motion [44]. The combination of these intramolecular pseudo-rotations with the standard rotations of the molecule leads to entangled  $\text{SO}(5)$  “superrotational motion” [45]. This complex and rich “hydrogen scrambling” dynamics remains unperturbed under helium solvation [46] in agreement with our present findings. Thirdly, an intricate coupling has recently been discovered between the complex rovibrational motion of  $\text{CH}_5^+$  and bosonic exchange in the *microsolvation limit* with up to only four  $^4\text{He}$  atoms [47].

We study quantum solvation and superfluid response of  $\text{CH}_5^+$  in  $^4\text{He}$  nanoclusters of up to 60 helium atoms and unveil a novel phenomenon that is unknown in the microsolvation limit. These results are referenced to  $\text{CH}_4$  in helium [39] to compare to this “ordinary cousin” of  $\text{CH}_5^+$ . Contrary to  $\text{CH}_5^+$ ,  $\text{CH}_4$  is a standard quasi-rigid molecule subject to small-amplitude motion that is well described by quasi-harmonic deviations from a unique equilibrium structure. Moreover, as most neutral species,  $\text{CH}_4$  does not feature such strong interactions as  $\text{CH}_5^+$  with helium.

## METHODS AND COMPUTATIONAL DETAILS

All simulations of  $\text{CH}_5^+$  and  $\text{CH}_4$  solvated in clusters composed of  $n = 1$  up to 60  $^4\text{He}$  atoms have been carried out at  $T = 0.5\text{ K}$  using finite temperature bosonic path integral techniques. This approach takes into account the full molecular flexibility at essentially converged coupled cluster level as recently reviewed in Ref. 48. Accordingly, we used a hybrid PIMD/ PIMC approach [49] in which helium is sampled using path integral Monte Carlo (PIMC) [50] to account for the bosonic nature of  $^4\text{He}$ , whereas the molecule is described using path integral molecular dynamics (PIMD). More precisely, the configuration and permutation space of bosonic helium is sampled using the continuous-space worm algorithm [51, 52] (in the specific canonical variant introduced in the appendix of Ref. 48), while the configuration space of the impurity is sampled using the path integral quantum thermal bath (PIQTB) technique [53] as adapted and validated for path integral simulations at very low temperatures [54]. Path integral convergence is achieved by describing the helium density matrix within the pair density approximation [50] using a high-temperature matrix computed at  $T = 80\text{ K}$  resulting in a path integral dis-

cretization of 160 beads at  $0.5\text{ K}$ , while the path integral is discretized using 640 beads for the molecule in conjunction with the PIQTB thermostat. The results reported here have been obtained by averaging over 20 independent runs propagated using a formal PIMD time step of  $0.25\text{ fs}$  for  $4 \cdot 10^5$  steps corresponding to a trajectory length of formally  $100\text{ ps}$  for each of the independent runs. Between two PIMD steps, helium was sampled using at least  $1 \cdot 10^5$  PIMC moves per helium atom. All interactions involving  $\text{CH}_5^+$  and  $\text{CH}_4$  are represented using highly accurate neural network potentials trained to essentially converged coupled cluster electronic structure calculations [55, 56]. We refer to the SM Sec. I for more information on the methodology of these neural network potentials as well as for comprehensive benchmarks.

To study the superfluid response of  $^4\text{He}$  around the molecule, we compute the superfluid fraction  $f_s$  of helium which quantifies the fraction of helium being in the superfluid state. Within the two-fluid model of superfluidity, the total helium density is divided into a superfluid density  $\rho_s$  and a normal density  $\rho_n$  and the superfluid fraction is then obtained as the ratio  $f_s = \rho_s/\rho_n$ . Various estimators have been developed to compute the superfluid fraction in path integral simulations. Here we use the so-called “area estimator” that has been developed specifically for finite size clusters [18] and which is based on the vectorial area of the exchange path, see Sec. III.A of the SM for more detailed information. One should note that this estimator is formally valid in the thermodynamic limit and in practice presents some limitations when dealing with very small clusters. In particular, it gives a non zero superfluid fraction for a single helium atom. This drawback can be corrected using a rescaled estimator, the so-called “exchange estimator” [29]. We carefully tested the validity of the area estimator in our case, see Sec. III.A and, Fig. S14 of the SM, by comparing to the exchange estimator.

Moreover, in order to get some local information about the superfluid response of helium, we estimate the local superfluid density  $\rho_s(\vec{r})$  in two different ways. The first estimator we use is based on the length of the exchange path. Indeed, it is well-known that superfluidity is related to the presence of long exchange path [57]. It is thus possible to estimate  $\rho_s(r)$  by computing the density of long exchange paths [30],  $\rho_s(\vec{r}) = \sum_{p>l}^{N_{\text{He}}} \rho_p(\vec{r})$ , where the sum runs over exchange paths exceeding a user-defined length of  $l$ . In this work, we chose  $l = 6$ , i.e. all exchange paths involving more than 6 atoms are considered to contribute to the superfluid density. We checked that the obtained superfluid densities remain qualitatively similar for different values of the cutoff length, see Sec. III.B and, in particular Fig. S16 of the SM. The second estimator we use to compute superfluid densities is a generalization of the area estimator of the superfluid fraction, see Sec. III.B of the SM for more details including the expression and its derivation.

## STRUCTURAL PROPERTIES

### Molecular Structure

The first question that arises is the impact of the solvent on the molecular properties, in particular their structure and dynamics. It is usually assumed that the impact of helium is negligible, due to the weak nature of its interaction with the molecule, and helium is thus considered one of the best solvents in particular for spectroscopic studies [16]. The question of the impact of helium on fluxional molecules, which exhibit fragile large-amplitude motion, has been recently studied for  $\text{CH}_5^+$  microsolvated with up to only four  $^4\text{He}$  atoms [58]. This study has revealed that the impact of helium on the molecular structure is indeed negligible even for the utmost fluxional  $\text{CH}_5^+$  molecule, and that helium does not seem to impact the fluxionality and large-amplitude motion. As clearly seen in the identical distribution functions for key structural properties of  $\text{CH}_4$  and  $\text{CH}_5^+$  in Fig. 1, the impact of helium remains negligible, even if the first helium solvation shell is fully closed with 16 helium atoms, probed here with  $n = 30$   $^4\text{He}$ . Moreover, no significant change in the molecular structure is observed when increasing the number of helium atoms even up to 60  $^4\text{He}$  around the molecule, in which case the molecule is entirely immersed in helium. Thus, the findings of Ref. 58 are not only valid in the extreme microsolvation limit but extend further to the fully solvated regime.

### Helium Solvation Structure

The impact of neutral and charged impurities on the surrounding helium is illustrated by the distributions reported in Fig. 2 for  $\text{CH}_4$  versus  $\text{CH}_5^+$  solvated by 60  $^4\text{He}$  atoms. The pronounced  $\text{CH}_5^+ \cdots ^4\text{He}$  interaction leads to large density modulations around the impurity and almost no interchange of helium atoms between the first and second solvation shell, as seen by the density close to zero in between the two peaks in Fig. 2(d). In contrast, the presence of  $\text{CH}_4$  leads to mild modulations even though a weakly defined, faint first shell can be identified followed by a region of significant helium density allowing for easy interchange of  $^4\text{He}$  between the first shell and beyond. These are the signatures of the much weaker interaction of  $^4\text{He}$  with  $\text{CH}_4$  compared to  $\text{CH}_5^+$  as a result of  $\text{CH}_5^+$  being a charged molecule. This significant impact of  $\text{CH}_5^+$  on the solvent structure can also be seen in the  $\text{He} \cdots \text{He}$  distributions that indicates a highly structured helium environment only around  $\text{CH}_5^+$  whereas not much such structure is seen for  $\text{CH}_4$ . This is most pronounced in the first shell, see inset of Fig. 2(e), where the high density of about  $0.11 \text{ \AA}^{-3}$ , which largely exceeds the freezing density of bulk helium, results in a solid-like order — the  $^4\text{He}$  snowball as known from simple

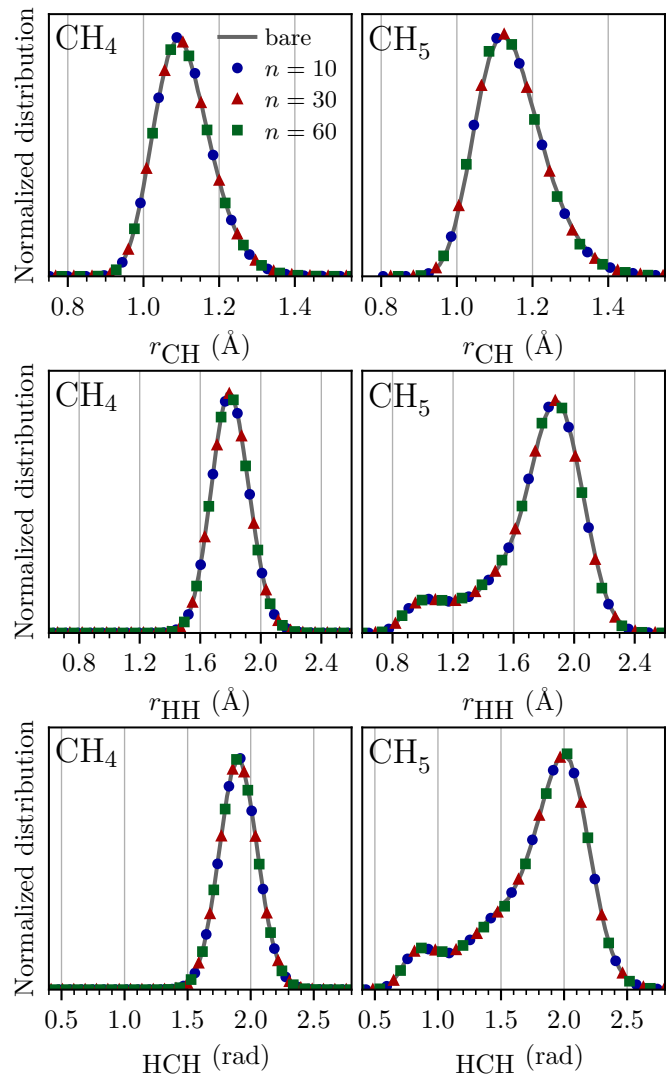


Figure 1. Molecular structure of  $\text{CH}_4$  (left column) and  $\text{CH}_5^+$  (right column) solvated by different numbers of helium atoms  $n$  (symbols) and compared to the isolated bare  $n = 0$  case (gray line) at  $T = 0.5 \text{ K}$ . The distributions of CH distances, HH distances and HCH angles are presented in the top, middle, and bottom panels, respectively.

monatomic cations. This solid-like structure of the first shell is confirmed by the angular distribution of helium around the carbon atom of  $\text{CH}_5^+$ , shown in the inset of Fig. 2(d), that exhibits sharp peaks in the first shell. Finally, the spatial distribution functions (SDFs) depicted in the rightmost column of Fig. 2 clearly summarize what is observed based on these radial and angular distribution functions. The real-space structuring of the probability distribution of  $^4\text{He}$  atoms around  $\text{CH}_5^+$  versus  $\text{CH}_4$  appears clearly:  $^4\text{He}$  atoms are significantly more localized around  $\text{CH}_5^+$  (f) compared to  $\text{CH}_4$  (c) which indicates *pronounced local translational and orientational order of helium close to  $\text{CH}_5^+$* . This is what we call “solid-like or-

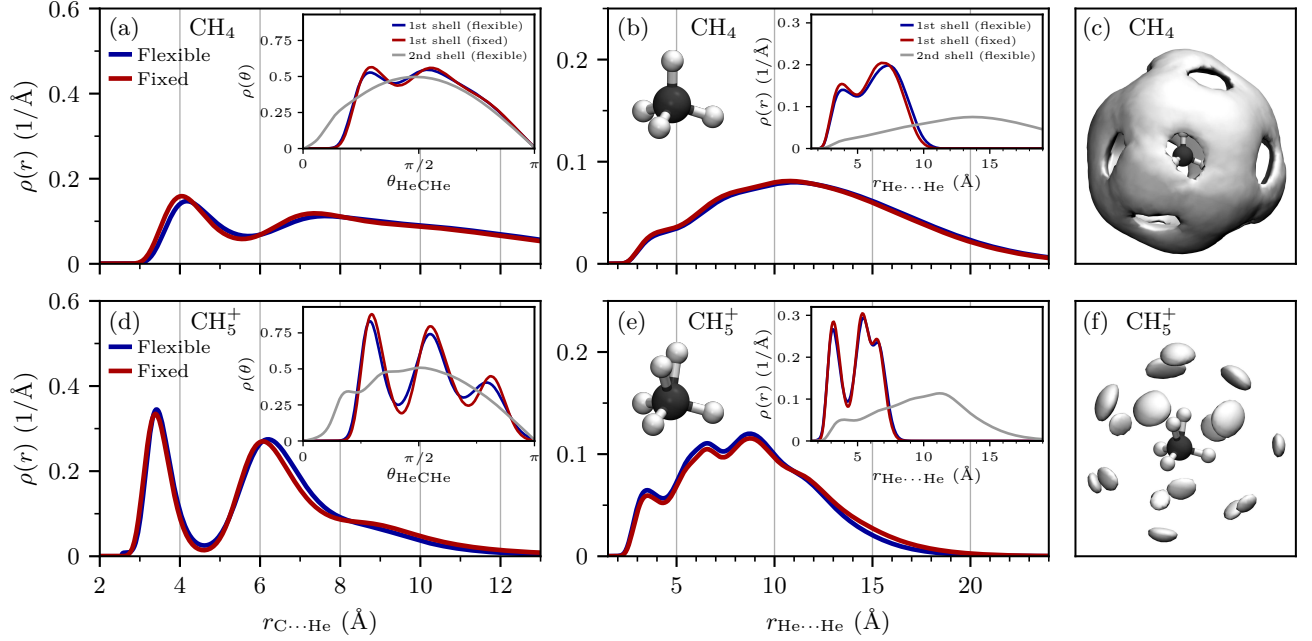


Figure 2. Distance distribution functions of C...He ((a) and (d)) and He...He ((b) and (e)) distances as well as spatial distribution functions (SDFs) of  $^4\text{He}$  around the impurities ((c) and (f)) for  $\text{CH}_4 \cdot ^4\text{He}_{60}$  (top row) and  $\text{CH}_5^+ \cdot ^4\text{He}_{60}$  (bottom row); data for the fully flexible and completely fixed impurities (with all constituting nuclei frozen as point-particles at their equilibrium structures as depicted in the insets of (b) and (e)) are shown in blue and red, respectively. The insets of (a) and (d) depict the angular distribution functions of  $^4\text{He}$  w.r.t. the carbon atom in the first and second (gray) shell, whereas the insets of (b) and (e) show the He...He distance distributions split into first and second (gray) shell. The SDFs have been computed w.r.t. fixed impurities using isovalues corresponding to a third of the respective maximum value which highlights the first  $^4\text{He}$  shell.

der” in such a finite cluster obviously without implying long-range periodicity as in an extended crystal.

Overall, this analysis of the helium structure reveals the presence of a frozen first shell around  $\text{CH}_5^+$ . In contrast, this phenomenon is not present for  $\text{CH}_4$ , in line with previous work [39], as supported by all data in panels (a) to (c) of Fig. 2. Interestingly, the ro-vibrational motion of the impurities, even of the strongly interacting  $\text{CH}_5^+$ , has negligible impact on the solvation shell structure for sufficiently large clusters (compare blue to red lines in Fig. 2). This behavior is different in small clusters (see SM Fig. S10), for which the molecular motion has a significant impact on the helium solvation structure. A pictorial summary of the structural differences is provided by the different SDFs in Fig. 2: While the 3D distribution of  $^4\text{He}$  around  $\text{CH}_4$  in panel (c) is broad and smeared out (“liquid-like”),  $^4\text{He}$  atoms are localized at well-defined position (“solid-like”) around  $\text{CH}_5^+$  in (f).

## SUPERFLUID PROPERTIES

How are these structural differences linked to the superfluid response of  $^4\text{He}$ ,  $f_s$ , as a function of the number  $n$  of  $^4\text{He}$  atoms? Within the two-fluid model of super-

fluidity, the superfluid fraction  $f_s$  is defined as the ratio between the superfluid density  $\rho_s$  and the total density  $\rho$ . It can be obtained directly from our quantum simulations and, in addition, spatially decomposed in terms of local shell contributions based on the radial superfluid density  $\rho_s(r)$ , see SM Sec. III for methods. Figure 3 shows the global superfluid fraction of the helium around  $\text{CH}_4$  and  $\text{CH}_5^+$  as a function of the number of helium atoms. For  $\text{CH}_4$ ,  $f_s$  increases with  $n$  before reaching a maximum at  $n = 9$  which corresponds to the maximum size for which all helium atoms mostly belong to the first shell, as shown in SM Fig. S12. After that,  $f_s$  drops initially due to the low density of additional helium atoms outside the first shell which hinders bosonic exchange. Upon filling the second shell,  $f_s$  increases again, reaching about 0.78 for the largest cluster. As for the helium densities, the ro-vibrational motion of  $\text{CH}_4$  has negligible impact on  $f_s$  around this quasi-rigid and weakly interacting molecule as fixing its nuclei (red diamonds compared to blue squares) does not change  $f_s$ . We note that we obtain very similar values of  $f_s$  at  $T = 0.3\text{ K}$  (flexible: 0.91, fixed: 0.88) as reported for 12 helium atoms around  $\text{CH}_4$  in Ref. 39.

The superfluid response around  $\text{CH}_5^+$  is distinctly different. Despite the strongly localized helium in the first



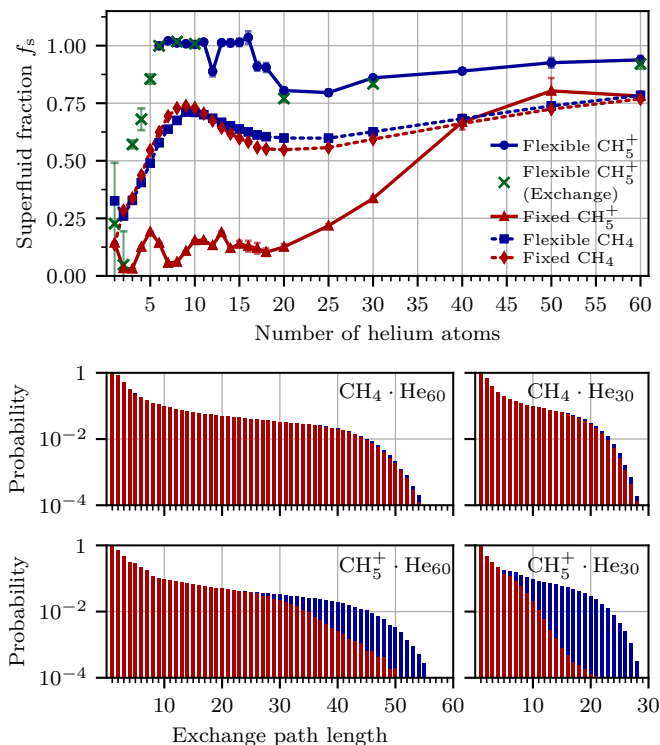


Figure 3. Top: Superfluid fraction  $f_s$  for  $\text{CH}_4 \cdot \text{He}_n$  (dashed lines) and  $\text{CH}_5^+ \cdot \text{He}_n$  (solid lines) as a function of  $n$ ; the “exchange estimator” has been used to compute the green crosses whereas all other data have been obtained from the “area estimator” as explained in SM Sec. III.A and validated in SM Fig. S14. Bottom: Probability of finding at least one exchange path of specific length for  $n = 60$  (left) and  $n = 30$  (right)  $^4\text{He}$  atoms. Data for flexible and fixed impurities (see caption of Fig. 2) are shown in blue and red, respectively; note that blue is superimposed by red where not visible.

shell, recall Fig. 2(f) versus (c), a large superfluid fraction, exceeding even the largest value obtained for the weakly interacting  $\text{CH}_4$ , is found around the  $\text{CH}_5^+$  impurity. Moreover, neglecting the ro-vibrational motion by fixing  $\text{CH}_5^+$  now greatly suppresses  $f_s$ , indicating almost no superfluid response for clusters of size lower than around 30  $^4\text{He}$  atoms (red triangles compared to blue circles) as expected from the traditional snowball picture. In the limit of large clusters, the *global* superfluid fraction tends to unity, which is expected regardless of the impurity since  $^4\text{He}$  is indeed superfluid at this temperature and we thus retrieve the bulk limit. In other words, for  $\text{CH}_4$ , the superfluid fraction does not change whether we fix the molecule in its equilibrium structure or not. This indicates that there is no impact of the ro-vibrational motion of  $\text{CH}_4$  on the superfluid response of the surrounding helium. In stark contrast, in the case of  $\text{CH}_5^+$ , the superfluid fraction values obtained when fixing the molecule in space are extremely small compared to the large values found when allowing for full flexibility of

the molecule. This shows that, in the case of protonated methane, the ro-vibrational motion of the molecule plays a crucial role and actually considerably enhances the superfluid response of the surrounding helium – despite the pronounced *local translational and orientational order of helium observed in the first shell around  $\text{CH}_5^+$* .

A deeper understanding can be obtained by studying the bosonic exchange path statistics for flexible versus fixed molecular impurities, see Fig. 3. The ro-vibrational motion of the fluxional  $\text{CH}_5^+$  significantly enhances bosonic exchange and facilitates long exchange cycles that are known to be related to superfluidity [30, 57]. No such impact on bosonic exchange is observed for the neutral  $\text{CH}_4$ .

Studying the evolution of the superfluid fraction with cluster size  $n \geq 6$  in Fig. 3, one can see that in the case of flexible  $\text{CH}_5^+$ ,  $f_s \approx 1$  for  $n = 6$  to 16 which corresponds to the first shell being completely filled (except for a drop at  $n = 12$  which is due to a known topological phenomenon as explained in the SM based on Fig. S15). After that, the value of  $f_s$  is slightly reduced due to the buildup of a second shell with a locally reduced  $^4\text{He}$  density that disfavors bosonic exchange. Upon increasing  $n$ , the second shell gets filled and  $f_s$  increases accordingly, reaching  $f_s \approx 0.9$  for  $n = 60$ , see SM Fig. S12 for shell filling analysis. Our analyses indicate that the first solvation shell of  $^4\text{He}$  around flexible  $\text{CH}_5^+$  features maximum superfluidity as quantified by  $f_s \approx 1$ . Such pronounced superfluid response is found despite the first shell being solid-like.

Spatially-resolved insights into the superfluid response of helium can be obtained by defining a local superfluid density  $\rho_s(r)$  as presented in Fig. 4 for two different local estimators; see SM Sec. III.B for an extended discussion and validation. Similarly to what was observed for the superfluid fraction, the ro-vibrational motion of  $\text{CH}_4$  has negligible impact on the superfluid density from the first shell up to the largest  $\text{C} \cdots \text{He}$  distances. For  $\text{CH}_5^+$ , a very different scenario is found: Essentially zero superfluid density is present in the first  $^4\text{He}$  shell around the fixed  $\text{CH}_5^+$  molecule compared to a significant superfluid response in the second shell as clearly seen in the shell-resolved integrated superfluid densities in Table I. This is a direct consequence of the solid-like order of the helium in the first shell – induced by the strong interactions of this cationic impurity with helium – that suppresses the long exchange cycles and thus the superfluid response. When accounting for the ro-vibrational motion of this molecule however, the superfluid response of the first shell considerably increases. These findings are consistent between the two different local estimators of superfluidity as presented in the top and bottom panel of Fig. 4 as well as Table I. The main difference between the two estimators is the extent of superfluidity, where the exchange path estimator yields overall lower estimates throughout compared to the area estimator. By con-

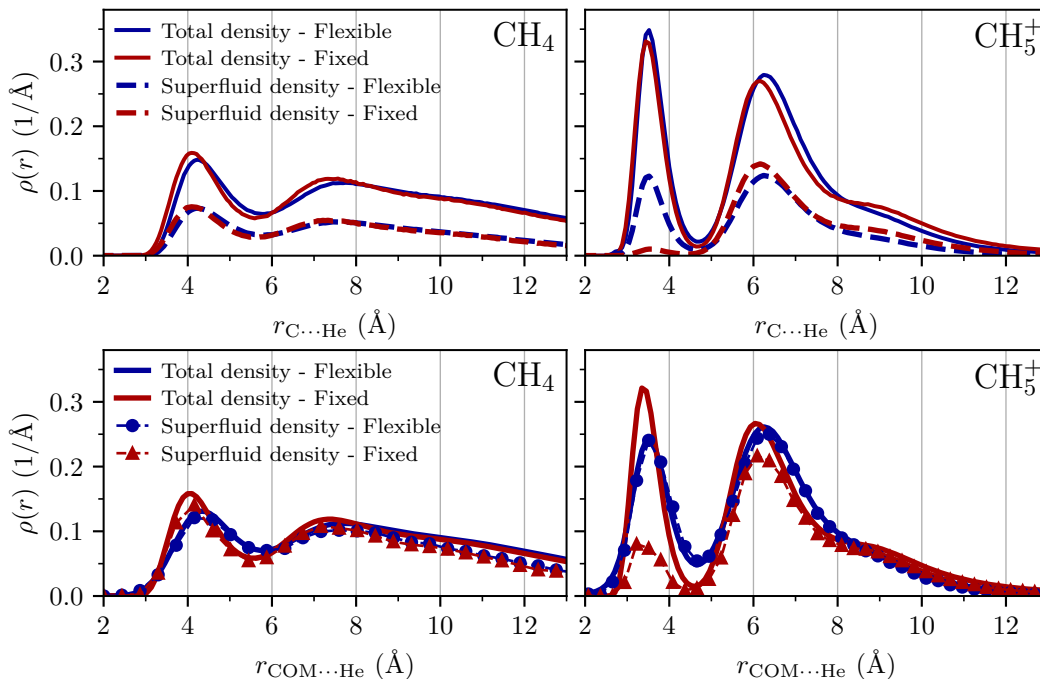


Figure 4. Local superfluid density  $\rho_s(r)$  computed using the “local exchange path estimator” (top row – dashed line) considering seven or more  $^4\text{He}$  atoms ( $l = 6$ ), and using the “local area path estimator” (bottom row – dashed line with symbols), together with the radial total density  $\rho(r)$  (full line). Data for the flexible and fixed impurities (see caption of Fig. 2) are shown in blue and red, respectively. Note that the definition of the radial density in the top and bottom panels is slightly different: in the top panels the distance  $r$  is defined with respect to the central Carbon atom of the molecule, while in the bottom panel it is with respect to the center of mass of the molecule as indicated in the axis labels.

struction the exchange path length estimator will always tend to underestimate the superfluid response while the area estimator is expected to overestimate it, so that ultimately the “real” superfluid density lies somewhere in between. For further details and an in-depth discussion we refer to SM Sec. III.B.

Importantly, this enhancement of the superfluid response of the first shell is not due to a decrease of the local solid-like order in the first shell as one could imagine, since the solvation structure is unaffected by the ro-vibrational molecular motion of  $\text{CH}_5^+$  as shown in Fig. 2. In a nutshell, in view of the strong localization of helium in the first shell around  $\text{CH}_5^+$ , one would expect almost no superfluid response as obtained around other strongly interacting impurities that lead to snowballs, and that is what is found when fixing that molecule in its equilibrium structure. However, including the full flexibility of  $\text{CH}_5^+$ , high superfluid fractions are found, in particular in the first shell, thus showing that the superfluid response of helium is induced by the ro-vibrational motion of this flexible molecule despite the pronounced localization of  $^4\text{He}$  close to this impurity.

We therefore conclude that helium in the first solvation shell around  $\text{CH}_5^+$  features *manifestations of supersolid behavior* (in the spirit of “*manifestations of superfluid behavior*” predicted long ago for *pure*  $^4\text{He}$  clusters [18])

Table I. Global superfluid fraction  $f_s$  and local superfluid fractions associated with the first and second solvation shells of  $\text{CH}_4 \cdot \text{He}_{60}$  and  $\text{CH}_5^+ \cdot \text{He}_{60}$  obtained by integrating the superfluid density computed using either the “local area estimator” or the “local exchange path estimator” with a cutoff length of  $l = 6$ , see SM Sec. III.B for details.

CH <sub>4</sub> ·He <sub>60</sub> – Flexible molecule			
	First shell	Second shell	Global
Exchange path	0.74	0.59	0.63
Area	0.96	0.83	0.86
CH <sub>4</sub> ·He <sub>60</sub> – Fixed molecule			
	First shell	Second shell	Global
Exchange path	0.72	0.59	0.63
Area	0.90	0.82	0.84
CH <sub>5</sub> <sup>+</sup> ·He <sub>60</sub> – Flexible molecule			
	First shell	Second shell	Global
Exchange path	0.54	0.63	0.61
Area	0.99	0.95	0.96
CH <sub>5</sub> <sup>+</sup> ·He <sub>60</sub> – Fixed molecule			
	First shell	Second shell	Global
Exchange path	0.04	0.55	0.42
Area	0.28	0.83	0.68

as indicated by pronounced bosonic exchange in combination with strong localization and spatial order of  $^4\text{He}$ . Evidently, the phenomenon uncovered here can only appear for clusters that are large enough to fully solvate the

impurity and is thus absent in the microsolvation limit.

Are there any prospects to experimentally probe our prediction? Manifestations of superfluid behavior in finite  $^4\text{He}$  clusters were first predicted based on seminal path integral simulations [18] and experimentally confirmed a decade later. This experimental confirmation of “*microscopic manifestation of superfluidity*” was made possible thanks to novel experimental ideas based on the IR spectra of a well-chosen molecular impurity used as probe of the local superfluidity in  $^4\text{He}$  clusters [15]. Concerning now manifestations of local supersolidity in  $\text{CH}_5^+\cdot\text{He}_n$  clusters, we refer to recent progress in measuring IR spectra of various charged molecules in helium clusters and nanodroplets [46, 59–61], notably also including  $\text{CH}_5^+$ . Similar to the original ideas behind what has been called the “microscopic Andronikashvili experiment” [15], IR spectra of  $\text{CH}_5^+$  in  $^3\text{He}$  versus  $^4\text{He}$  nanodroplets as well as addition of a few  $^4\text{He}$  atoms to  $\text{CH}_5^+$  in  $^3\text{He}$  could reveal insightful differences. Challenges certainly arise regarding IR spectroscopy of  $\text{CH}_5^+$  since the molecule is known to stay fluxional in helium [46, 47, 58] thus retaining its notorious spectroscopic complexity [62]. Exploring alternative observables different from IR spectra might therefore provide complementary avenues for future experimental searches for this local supersolidity in doped  $\text{He}^4$  clusters potentially based on experimental ideas that are yet to be developed.

## CONCLUSIONS AND OUTLOOK

This study provides strong evidence for manifestations of local supersolid behavior of  $^4\text{He}$  around a charged molecular impurity, namely  $\text{CH}_5^+$ . On the one hand, the strong interactions between this molecular cation and helium lead to the long known snowball effect, meaning a solid-like arrangement of helium in the first shell with well-localized  $^4\text{He}$  density. On the other hand, the strongly localized atoms in this shell are involved in vivid bosonic exchange, induced by the ro-vibrational motion of this fluxional molecular impurity, in particular the fast and complex rotational motion emerging from the intimate coupling of overall rotations and intramolecular pseudo-rotations. The combination of strong  $^4\text{He}$  localization in the first shell with pronounced bosonic exchange therein, leading to an intense superfluid response, thus clearly indicates manifestations of local supersolid behavior of  $^4\text{He}$  close to suitable molecular impurities – akin to the long-known manifestations of microscopic superfluidity in doped helium nanodroplets.

We expect this impurity-induced local supersolid response to appear in bosonic clusters doped with other impurities featuring a strong interaction with the solvent combined with fast rotations resulting in a significant coupling between the impurity and the solvent. In particular, due to the stronger interactions of most impu-

rities with para- $\text{H}_2$ , we believe that the effect uncovered here could appear as well in finite para- $\text{H}_2$  clusters doped with molecular impurities. The phenomenon is however markedly different from the supersolidity that has long been predicted in pure para- $\text{H}_2$  clusters of specific sizes, since the local supersolid behavior is induced here by the molecular impurity and is also not limited to magic numbers. Moreover, since the effect uncovered here can be expected to appear with various molecular ions in helium or other bosonic quantum fluids, it would be highly interesting to explore in particular whether doping with an assembly of molecular ions serving as seeds could lead to new supersolid phases especially in bulk helium or para-hydrogen.

## ACKNOWLEDGMENTS

We are thankful to Harald Forbert and Felix Uhl for many insightful discussions. This work was partially supported by DFG via MA 1547/19 and also funded by the *Deutsche Forschungsgemeinschaft* (DFG, German Research Foundation) under Germany’s Excellence Strategy – EXC 2033 – 390677874. C.S. acknowledges partial financial support from the Alexander von Humboldt-Stiftung and the DFG project number 500244608. The computational resources were provided by HPC@ZEMOS, HPC-RESOLV, and BoViLab@RUB.

---

\* [fabien.brieuc@cea.fr](mailto:fabien.brieuc@cea.fr)

† [christoph.schran@rub.de](mailto:christoph.schran@rub.de)

‡ [dominik.marx@rub.de](mailto:dominik.marx@rub.de)

- [1] A. J. Leggett, Can a Solid Be “Superfluid”?, *Phys. Rev. Lett.* **25**, 1543 (1970).
- [2] M. Boninsegni and N. V. Prokof’ev, Colloquium: Supersolids: What and where are they?, *Rev. Mod. Phys.* **84**, 759 (2012).
- [3] A. F. Andreev and I. M. Lifshitz, Quantum Theory of Defects in Crystals, *Sov. Phys. JETP* **29**, 1107 (1969).
- [4] L. Reatto, Bose-Einstein Condensation for a Class of Wave Functions, *Phys. Rev.* **183**, 334 (1969).
- [5] J.-R. Li, J. Lee, W. Huang, S. Burchesky, B. Shteynas, F. C. Top, A. O. Jamison, and W. Ketterle, A stripe phase with supersolid properties in spin-orbit-coupled Bose-Einstein condensates, *Nature* **543**, 91 (2017).
- [6] M. A. Norcia, C. Politi, L. Klaus, E. Poli, M. Sohmen, M. J. Mark, R. N. Bisset, L. Santos, and F. Ferlaino, Two-dimensional supersolidity in a dipolar quantum gas, *Nature* **596**, 357 (2021).
- [7] T. Bland, E. Poli, C. Politi, L. Klaus, M. A. Norcia, F. Ferlaino, L. Santos, and R. N. Bisset, Two-Dimensional Supersolid Formation in Dipolar Condensates, *Phys. Rev. Lett.* **128**, 195302 (2022).
- [8] C. W. Myung, B. Hirshberg, and M. Parrinello, Prediction of a Supersolid Phase in High-Pressure Deuterium, *Phys. Rev. Lett.* **128**, 045301 (2022).

- [9] P. Sindzingre, D. M. Ceperley, and M. L. Klein, Superfluidity in clusters of p-H<sub>2</sub> molecules, *Phys. Rev. Lett.* **67**, 1871 (1991).
- [10] F. Mezzacapo and M. Boninsegni, On the Possible “Supersolid” Character of Parahydrogen Clusters, *J. Phys. Chem. A* **115**, 6831–6837 (2011).
- [11] E. Kim and M. H. W. Chan, Probable observation of a supersolid helium phase, *Nature* **427**, 225 (2004).
- [12] S. Balibar, The enigma of supersolidity, *Nature* **464**, 176 (2010).
- [13] D. Y. Kim and M. H. W. Chan, Absence of Supersolidity in Solid Helium in Porous Vycor Glass, *Phys. Rev. Lett.* **109**, 155301 (2012).
- [14] J. Choi, A. A. Zadorozhko, J. Choi, and E. Kim, Spatially Modulated Superfluid State in Two-Dimensional <sup>4</sup>He Films, *Phys. Rev. Lett.* **127**, 135301 (2021).
- [15] S. Grebenev, J. P. Toennies, and A. F. Vilesov, Superfluidity Within a Small Helium-4 Cluster: The Microscopic Andronikashvili Experiment, *Science* **279**, 2083 (1998).
- [16] J. P. Toennies and A. F. Vilesov, Spectroscopy of atoms and molecules in liquid helium, *Annu. Rev. Phys. Chem.* **49**, 1 (1998).
- [17] J. P. Toennies and A. F. Vilesov, Superfluid Helium Droplets: A Uniquely Cold Nanomatrix for Molecules and Molecular Complexes, *Angew. Chem. Int. Ed.* **43**, 2622 (2004).
- [18] P. Sindzingre, M. L. Klein, and D. M. Ceperley, Path-integral Monte Carlo study of low-temperature <sup>4</sup>He clusters, *Phys. Rev. Lett.* **63**, 1601 (1989).
- [19] K. R. Atkins, Ions in Liquid Helium, *Phys. Rev.* **116**, 1339 (1959).
- [20] A. Nakayama and K. Yamashita, Theoretical study on the structure of Na<sup>+</sup>-doped helium clusters: Path integral Monte Carlo calculations, *J. Chem. Phys.* **112**, 10966 (2000).
- [21] M. Buzzacchi, D. E. Galli, and L. Reatto, Alkali ions in superfluid <sup>4</sup>He and structure of the snowball, *Phys. Rev. B* **64**, 094512 (2001).
- [22] D. E. Galli, D. M. Ceperley, and L. Reatto, Path Integral Monte Carlo Study of <sup>4</sup>He Clusters Doped with Alkali and Alkali-Earth Ions, *J. Phys. Chem. A* **115**, 7300 (2011).
- [23] J. Poitrenaud and F. I. B. Williams, Precise Measurement of Effective Mass of Positive and Negative Charge Carriers in Liquid Helium II, *Phys. Rev. Lett.* **29**, 1230 (1972).
- [24] S. Müller, M. Mudrich, and F. Stienkemeier, Alkali-helium snowball complexes formed on helium nanodroplets, *J. Chem. Phys.* **131**, 044319 (2009).
- [25] P. Bartl, C. Leidlmair, S. Denifl, P. Scheier, and O. Echt, On the Size and Structure of Helium Snowballs Formed around Charged Atoms and Clusters of Noble Gases, *J. Phys. Chem. A* **118**, 8050 (2014).
- [26] F. J. Bartis, The mobility of positive ions with large He I halos, *Phys. Lett. A* **60**, 417 (1977).
- [27] J. Tang, Y. Xu, A. R. W. McKellar, and W. Jäger, Quantum Solvation of Carbonyl Sulfide with Helium Atoms, *Science* **297**, 2030 (2002).
- [28] Y. Xu, W. Jäger, J. Tang, and A. R. W. McKellar, Spectroscopic Studies of Quantum Solvation in <sup>4</sup>He<sub>N</sub>-N<sub>2</sub>O Clusters, *Phys. Rev. Lett.* **91**, 163401 (2003).
- [29] A. R. W. McKellar, Y. Xu, and W. Jäger, Spectroscopic Exploration of Atomic Scale Superfluidity in Doped Helium Nanoclusters, *Phys. Rev. Lett.* **97**, 183401 (2006).
- [30] Y. Kwon and K. B. Whaley, Atomic-Scale Quantum Solvation Structure in Superfluid Helium-4 Clusters, *Phys. Rev. Lett.* **83**, 4108 (1999).
- [31] E. W. Draeger and D. M. Ceperley, Superfluidity in a Doped Helium Droplet, *Phys. Rev. Lett.* **90**, 065301 (2003).
- [32] S. Moroni, A. Sarsa, S. Fantoni, K. E. Schmidt, and S. Baroni, Structure, Rotational Dynamics, and Superfluidity of Small OCS-Doped He Clusters, *Phys. Rev. Lett.* **90**, 143401 (2003).
- [33] J. Tang, A. R. W. McKellar, F. Mezzacapo, and S. Moroni, Bridging the Gap between Small Clusters and Nanodroplets: Spectroscopic Study and Computer Simulation of Carbon Dioxide Solvated with Helium Atoms, *Phys. Rev. Lett.* **92**, 145503 (2004).
- [34] F. Paesani, Y. Kwon, and K. B. Whaley, Onset of Superfluidity in Small CO<sub>2</sub>(<sup>4</sup>He)<sub>N</sub> Clusters, *Phys. Rev. Lett.* **94**, 153401 (2005).
- [35] C. C. Duminuco, D. E. Galli, and L. Reatto, Local solid order around impurities: doped clusters and ions in <sup>4</sup>He, *Physica B: Condens. Matter* **284–288**, 109 (2000).
- [36] Y. Kwon, P. Huang, M. V. Patel, D. Blume, and K. B. Whaley, Quantum solvation and molecular rotations in superfluid helium clusters, *J. Chem. Phys.* **113**, 6469 (2000).
- [37] N. Blinov, X. Song, and P.-N. Roy, Path integral Monte Carlo approach for weakly bound van der Waals complexes with rotations: Algorithm and benchmark calculations, *J. Chem. Phys.* **120**, 5916 (2004).
- [38] R. E. Zillich, F. Paesani, Y. Kwon, and K. B. Whaley, Path integral methods for rotating molecules in superfluids, *J. Chem. Phys.* **123**, 114301 (2005).
- [39] N. D. Markovskiy and C. H. Mak, Path Integral Studies of the Rotations of Methane and Its Heavier Isotopomers in <sup>4</sup>He Nanoclusters, *J. Phys. Chem. A* **113**, 9165 (2009).
- [40] Y. Kwon and H. Shin, Superfluidity and structural order in <sup>4</sup>He adsorbed on a C<sub>20</sub> molecule: Path-integral Monte Carlo calculations, *Phys. Rev. B* **82**, 172506 (2010).
- [41] P. A. Crowell and J. D. Reppey, Superfluidity and film structure in <sup>4</sup>He adsorbed on graphite, *Phys. Rev. B* **53**, 2701 (1996).
- [42] J. Nyéki, A. Phillis, B. Cowan, and J. Saunders, On the ‘Supersolid’ Response of the Second Layer of <sup>4</sup>He on Graphite, *J. Low Temp. Phys.* **187**, 475 (2017).
- [43] J. Nyéki, A. Phillis, A. Ho, D. Lee, P. Coleman, J. Parpia, B. Cowan, and J. Saunders, Intertwined superfluid and density wave order in two-dimensional <sup>4</sup>He, *Nat. Phys.* **13**, 455 (2017).
- [44] D. Marx and M. Parrinello, Structural quantum effects and three-centre two-electron bonding in CH<sub>3</sub><sup>+</sup>, *Nature* **375**, 216 (1995).
- [45] H. Schmiedt, P. Jensen, and S. Schlemmer, Collective Molecular Superrotation: A Model for Extremely Flexible Molecules Applied to Protonated Methane, *Phys. Rev. Lett.* **117**, 223002 (2016).
- [46] J. Davies, S. Yang, and A. M. Ellis, Infrared spectra of carbocations and CH<sub>4</sub><sup>+</sup> in helium, *Phys. Chem. Chem. Phys.* **23**, 27449 (2021).
- [47] F. Uhl and D. Marx, Quantum Microsolvation of Protonated Methane with <sup>4</sup>He: Large-Amplitude Motion Heavily Influences Bosonic Exchange, *Phys. Rev. Lett.* **123**, 123002 (2019).
- [48] F. Briec, C. Schran, F. Uhl, H. Forbert, and D. Marx, Converged quantum simulations of reactive solutes in



- superfluid helium: The Bochum perspective, *J. Chem. Phys.* **152**, 210901 (2020).
- [49] L. Walewski, H. Forbert, and D. Marx, Reactive path integral quantum simulations of molecules solvated in superfluid helium, *Comput. Phys. Commun.* **185**, 884 (2014).
- [50] D. M. Ceperley, Path integrals in the theory of condensed helium, *Rev. Mod. Phys.* **67**, 279 (1995).
- [51] M. Boninsegni, N. Prokof'ev, and B. Svistunov, Worm Algorithm for Continuous-Space Path Integral Monte Carlo Simulations, *Phys. Rev. Lett.* **96**, 070601 (2006).
- [52] M. Boninsegni, N. V. Prokof'ev, and B. V. Svistunov, Worm algorithm and diagrammatic Monte Carlo: A new approach to continuous-space path integral Monte Carlo simulations, *Phys. Rev. E* **74**, 036701 (2006).
- [53] F. Brieuc, H. Dammak, and M. Hayoun, Quantum Thermal Bath for Path Integral Molecular Dynamics Simulation, *J. Chem. Theory Comput.* **12**, 1351 (2016).
- [54] C. Schran, F. Brieuc, and D. Marx, Converged Colored Noise Path Integral Molecular Dynamics Study of the Zundel Cation down to Ultralow Temperatures at Coupled Cluster Accuracy, *J. Chem. Theory Comput.* **14**, 5068 (2018).
- [55] C. Schran, F. Uhl, J. Behler, and D. Marx, High-dimensional neural network potentials for solvation: The case of protonated water clusters in helium, *J. Chem. Phys.* **148**, 102310 (2017).
- [56] C. Schran, J. Behler, and D. Marx, Automated Fitting of Neural Network Potentials at Coupled Cluster Accuracy: Protonated Water Clusters as Testing Ground, *J. Chem. Theory Comput.* **16**, 88 (2020).
- [57] W. Krauth, Quantum Monte Carlo Calculations for a Large Number of Bosons in a Harmonic Trap, *Phys. Rev. Lett.* **77**, 3695 (1996).
- [58] F. Uhl and D. Marx, Helium Tagging of Protonated Methane in Messenger Spectroscopy: Does It Interfere with the Fluxionality of  $\text{CH}_5^+$ ?, *Angew. Chem. Int. Ed.* **57**, 14792 (2018).
- [59] J. A. Davies, N. A. Besley, S. Yang, and A. M. Ellis, Probing Elusive Cations: Infrared Spectroscopy of Protonated Acetic Acid, *J. Phys. Chem. Lett.* **10**, 2108 (2019).
- [60] S. Erukala, D. Verma, and A. Vilesov, Rotation of  $\text{CH}_3^+$  Cations in Helium Droplets, *J. Phys. Chem. Lett.* **12**, 5105 (2021).
- [61] J. Davies, C. Schran, F. Brieuc, D. Marx, and A. M. Ellis, Onset of Rotational Decoupling for a Molecular Ion Solvated in Helium: From Tags to Rings and Shells, *Phys. Rev. Lett.* **130**, 083001 (2023).
- [62] O. Asvany, P. Padma Kumar, B. Redlich, I. Hegemann, S. Schlemmer, and D. Marx, Understanding the Infrared Spectrum of Bare  $\text{CH}_5^+$ , *Science* **309**, 1219 (2005).

**Supplemental Material to  
Manifestations of Local Supersolidity of  $^4\text{He}$   
around a Charged Molecular Impurity**

Fabien Brieuc,<sup>1,2,\*</sup> Christoph Schran,<sup>1,3,†</sup> and Dominik Marx<sup>1,‡</sup>

<sup>1</sup>*Lehrstuhl für Theoretische Chemie, Ruhr-Universität Bochum, 44780 Bochum, Germany*

<sup>2</sup>*Present address: Laboratoire Matière en Conditions Extrêmes, Université Paris-Saclay,  
CEA, 91680 Bruyères-le-Châtel; CEA, DAM, DIF, F-91297 Arpajon, France*

<sup>3</sup>*Present address: Yusuf Hamied Department of Chemistry,  
University of Cambridge, Lensfield Road, Cambridge CB2 1EW, UK*

(Dated: August 15, 2023)

---

\* [fabien.brieuc@cea.fr](mailto:fabien.brieuc@cea.fr)

† [christoph.schran@rub.de](mailto:christoph.schran@rub.de)

‡ [dominik.marx@rub.de](mailto:dominik.marx@rub.de)

## CONTENTS

I. Neural Networks Potentials	3
A. Methodology	3
B. Potential Energy Surface of $\text{CH}_5^+$	3
C. Potential Energy Surface of $\text{CH}_4$	7
D. $\text{CH}_5^+ \cdots \text{Helium}$ Interaction	9
E. $\text{CH}_4 \cdots \text{Helium}$ Interaction	12
II. Solvation Shell Structure	13
III. Superfluid Estimators	17
A. Superfluid Fraction	17
B. Local Superfluid Density	22
C. Microsolvation Limit	25
References	28

## I. NEURAL NETWORKS POTENTIALS

### A. Methodology

High-dimensional NNPs [1, 2] have been fitted against coupled cluster reference calculations including singles, doubles and perturbative triple excitations, CCSD(T). The augmented correlation-consistent basis set up to triple zeta functions [3, 4] (aug-cc-pVTZ or AVTZ) has been used in combination with the explicitly correlated F12a method [5, 6] using an adequate scaling of the triples [6] (providing CCSD(T\*)-F12a/AVTZ which is referred to simply as “CC” in the following), leading to a description of the electronic structure that is essentially converged to the complete basis set limit. All reference calculations have been performed with the Molpro software package version 2012.1 [7]. The iterative procedure described in Refs. 8 and 9 was used to optimally build the training sets of the models, while ensuring that only a minimum number of reference calculations were performed. All atomic neural networks have a fully connected feed-forward architecture composed of two hidden layers of 25 nodes each using a hyperbolic tangent as the activation function. The output layer contains only one neuron activated by a linear function as usual for regression. Training of the models was performed with the RuNNer program [10] using the element-decoupled Kalman filter optimizer [11]. The local atomic environments used as input of the models are described by atom-centered symmetry functions [12]. We refer to the supporting file `nnp-parameters.pdf` where all parameters of all neural network potentials as used in this study are provided.

The interactions between the molecules and helium are described by separate NNPs that were fitted to reproduce the impurity...He interaction in a pair-wise manner [8]. The reference interaction energies have been computed at the same level of theory as for the PESs of the molecules, but using the supermolecule approach and a counterpoise correction (cp) to correct for the basis set superposition error [13] (thus providing the CCSD(T\*)-F12a-AVTZcp method, which we also refer to as “CC” for simplicity in what follows). The scaling correction of the triple excitations has been applied in a system-size-consistent manner [14] by determining the correction only from the supermolecular cluster.

### B. Potential Energy Surface of $\text{CH}_5^+$

The training of the NNP to describe the PES of  $\text{CH}_5^+$ , thus providing what we call the NN-PES (NN-PES-CH5P-2022-V0), was performed on a training set composed of 18266 configurations as sampled by our automated fitting procedure from MD with classical nuclei and PIMD simulations



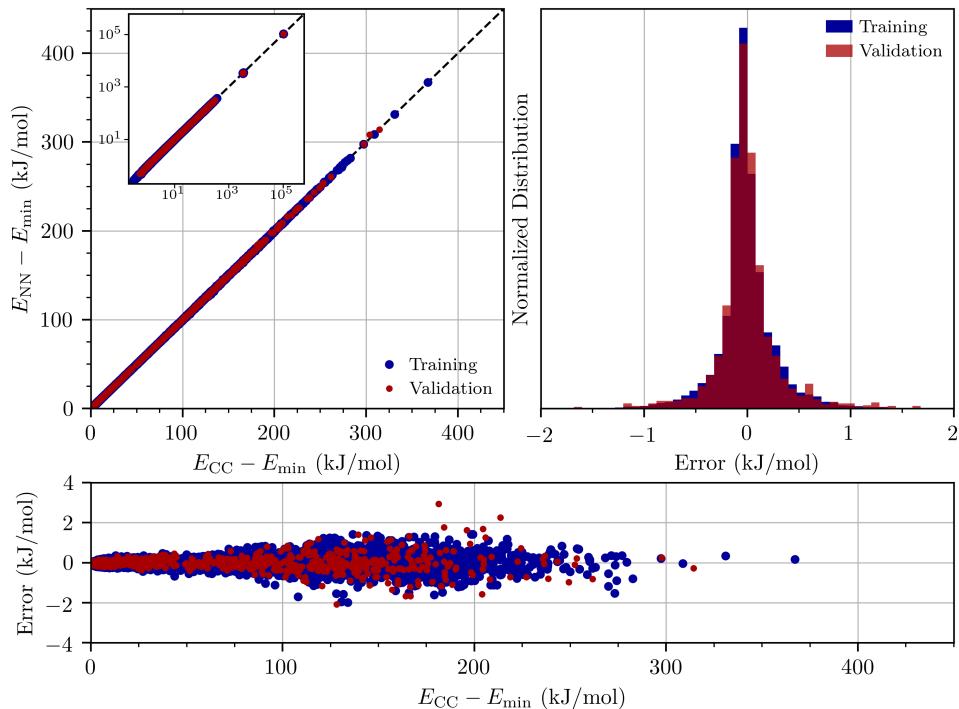


Figure S1. Analysis of the training of the  $\text{CH}_5^+$  NN-PES. Correlations of the energies obtained by the NN-PES (NN) and the reference coupled cluster (CC) method (top left). Histogram (top right) and values (bottom) of the associated errors. The energies are reported relative to the energy of the global minimum  $E_{\min}$ .

considering nuclear quantum effects at various temperatures ranging from 1 up to 1500 K. A limited amount of  $\text{CH}_3^+$  and  $\text{H}_2$  configurations were added in order to correctly describe configurations that are close to the dissociation channel (adding up to 800  $\text{CH}_3^+$  and 32  $\text{H}_2$  representative structures). Ten percent of the dataset is used as a validation set to assess the quality of the fit and to detect overfitting. The root mean square error (RMSE) obtained for the training and validation set is 0.3 and 0.4 kJ/mol, respectively, and the overall high quality of the training is illustrated in Fig. S1. The final NN-PES has been validated by investigating important stationary-point structures of protonated methane represented by the minimum energy structure and the lowest two saddle points depicted in Fig. S2. The global minimum energy structure of  $\text{CH}_5^+$  has an eclipsed  $\text{C}_s$  (e- $\text{C}_s$ ) point symmetry and is composed of a  $\text{CH}_3$  tripod and a  $\text{H}_2$  moiety connected through a three-center two-electron bond [15]. This  $\text{H}_2$  moiety can rotate around the  $\text{C}_3$  axis of the tripod, a motion associated to a stationary point with staggered  $\text{C}_s$  (s- $\text{C}_s$ ) symmetry and a small energy barrier that makes this pseudo-rotation essentially barrier-free. The second low-lying stationary point has the  $\text{C}_{2v}$  symmetry and is associated with another pseudo-rotation that connects two degenerate

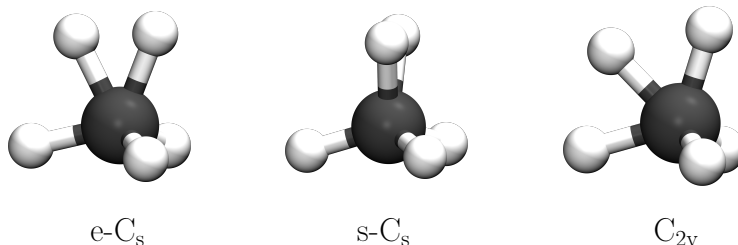


Figure S2. Important structures of  $\text{CH}_5^+$ : minimum energy (left), first stationary point (center) and second stationary point (right).

Table SI. Energy difference  $\Delta E(X) = E(X) - E(\text{e-C}_s)$  in kJ/mol as obtained using the NN-PES and the reference CC method with associated errors.

$X$	NN	CC	Error
s- $\text{C}_s$	0.3855	0.4296	0.0441
$\text{C}_{2v}$	3.817	3.6559	-0.1611

e- $\text{C}_s$  structures involving different atoms in the moiety. The combination of these two pseudo-rotations leads to a large-amplitude motion, sometimes called scrambling motion, that makes all the hydrogen atoms dynamically equivalent. Since this scrambling motion is associated with tiny energy barriers that are overcome by zero-point energy,  $\text{CH}_5^+$  exhibits large-amplitude motion even in the  $T \rightarrow 0$  limit: Protonated methane is the typical example of a quantum fluxional molecule.

Geometry optimizations of these different structures of  $\text{CH}_5^+$  have been performed using both, the NN-PES and explicit CC reference calculations. Their relative energies are compared in Table SI in order to confirm that the energy barriers associated with the large amplitude motion of protonated methane are correctly reproduced by the NN-PES. In particular, these tests show that the NN-PES represents the stationary points of  $\text{CH}_5^+$  on its complex PES to very high precision which greatly exceeds “chemical accuracy”. Moreover, the normal mode frequencies of  $\text{CH}_5^+$  in the minimum energy structure have been computed with the NN-PES and are compared in Table SII to the values obtained with the CC reference method. Also here, the NN-PES is able to reproduce the CC reference within a few  $\text{cm}^{-1}$ , highlighting the quality of this approach.

Finally, in order to test further the NN-PES on structures actually sampled in realistic simulations, we randomly extracted short pieces of MD and PIMD trajectories of a single  $\text{CH}_5^+$  in the gas phase in which the potential energy was evaluated using both the NN-PES and the CC reference method as depicted in Fig. S3. Independent of whether the nuclei are described as classical point particles or including nuclear quantum effects, the NN-PES provides perfect agreement with

Table SII. Normal mode frequencies in  $\text{cm}^{-1}$  in the minimum energy  $\text{e-C}_s$  structure of  $\text{CH}_5^+$  as obtained using the NN-PES and the reference CC method with associated errors. The mean absolute deviation (MAD) is also reported on the last line.

NN	226.48	831.19	1284.52	1301.37	1460.18	1482.71	1590.29	2436.55	2720.25	3004.74	3135.13	3238.15
CC	211.92	828.23	1282.81	1289.30	1461.79	1490.27	1595.63	2449.88	2713.51	3014.75	3133.99	3228.55
Error	-14.56	-2.96	-1.71	-12.1	1.61	7.56	5.34	13.3	-6.74	10.0	-1.14	-9.60
MAD	7.2											

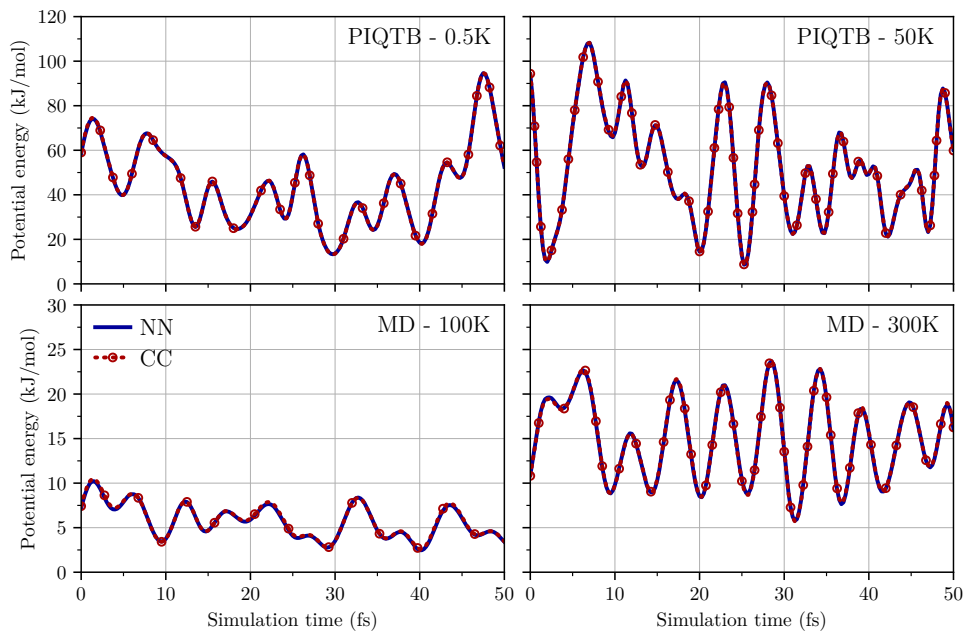


Figure S3. Potential energy of an isolated  $\text{CH}_5^+$  molecule along one replica of PIQTB trajectories (first row) at  $T = 0.5\text{K}$  (left) and  $50\text{K}$  (right) and along a standard MD trajectory (second row) at  $T = 100\text{K}$  (left) and  $300\text{K}$  (right). The coupled cluster reference data (CC) were obtained by recomputing the energies at each step of the NN-PES trajectories and are shown as red dashed lines (with only a few circles added since the CC energies practically superimpose the NN-PES data). All energies are reported relative to the energy of the global minimum ( $\text{e-C}_s$ ).

the CC reference energies covering very different temperature regimes. These various tests clearly highlight the outstanding quality of this NN-PES of  $\text{CH}_5^+$  that essentially allows for a description of the molecule at converged coupled cluster accuracy.

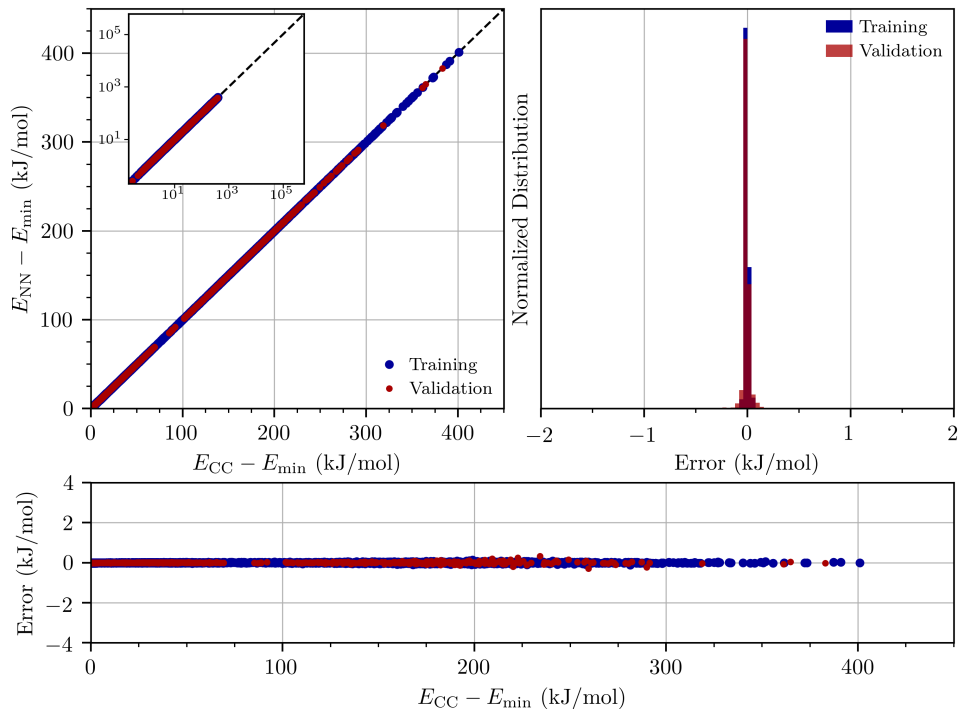


Figure S4. Analysis of the training of the  $\text{CH}_4$  NN-PES. Correlations of the energies obtained by the NN-PES (NN) and the reference coupled cluster (CC) method (top left). Histogram (top right) and values (bottom) of the associated errors. The energies are reported relative to the energy of the global minimum  $E_{\min}$ . We employ here on purpose the same scale as used for the validation of the  $\text{CH}_5^+$  NN-PES analyzed in Fig. S1 in order to allow for one-to-one comparison of this two cases which represent quasi-rigid ( $\text{CH}_4$ ) and highly fluxional ( $\text{CH}_5^+$ ) molecules of very similar kind and size.

### C. Potential Energy Surface of $\text{CH}_4$

The NN-PES of  $\text{CH}_4$  (NN-PES-CH4-2022-V0) has been developed following the same automated fitting procedure as used for  $\text{CH}_5^+$ . The dataset generated here is composed of 9245 configurations which have been selected from both PIMD and MD trajectories of isolated  $\text{CH}_4$  at temperatures ranging from 1.67 up to 1000 K. The RMSE associated with the training of the NN-PES are 0.02 kJ/mol the training set and 0.03 kJ/mol for the validation set. The quality of the fit is further illustrated in Fig. S4 at the level of errors, which clearly highlights that fitting the NN-PES of such a quasi-rigid and symmetric molecule as  $\text{CH}_4$  is a much easier task than fitting the complex PES of highly fluxional molecules such as  $\text{CH}_5^+$ . The minimum energy structure is very well reproduced with an error on the energy that is lower than 0.05 kJ/mol and errors on the associated normal modes of around  $1 \text{ cm}^{-1}$  only, as compiled in Table SIII. As for  $\text{CH}_5^+$ , the quality of the NN-



PES is further tested on short parts of representative MD and PIMD trajectories obtained using the NN-PES for which the potential energy gets re-evaluated using the reference CC method, see Fig. S5. For all these validation simulations – including various temperatures and both classical and quantum nuclei – essentially perfect agreement between the NN-PES and the CC reference is observed.

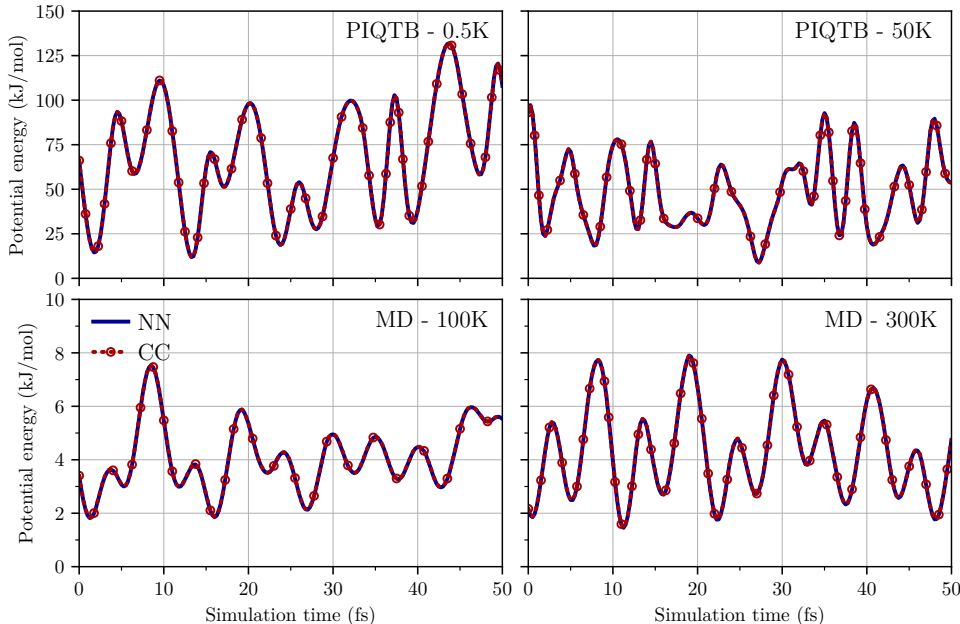


Figure S5. Potential energy of an isolated  $\text{CH}_4$  molecule along one replica of PIQTB trajectories (first row) at  $T = 0.5\text{ K}$  (left) and  $50\text{ K}$  (right) and along a standard MD trajectory (second row) at  $T = 100\text{ K}$  (left) and  $300\text{ K}$ . The coupled cluster reference data (CC) were obtained by recomputing the energies at each step of the NN-PES trajectories and are shown as red dashed lines (with only a few circles added since the CC energies practically superimpose the NN-PES data). All energies are reported relative to the energy of the global minimum.

Table SIII. Normal mode frequencies in  $\text{cm}^{-1}$  in the minimum energy structure of  $\text{CH}_4$  as obtained using the NN-PES and the reference CC method with associated errors. The mean absolute deviation (MAD) is also reported on the last line.

NN	1344.04	1344.04	1344.04	1568.65	1568.65	3036.86	3156.00	3156.00	3156.00
CC	1343.20	1343.32	1343.37	1568.09	1568.20	3032.68	3155.17	3155.26	3155.36
Error	-0.84	-0.72	-0.67	-0.56	-0.45	-4.18	-0.83	-0.78	-0.64
MAD	1.1								

### D. $\text{CH}_5^+ \cdots \text{Helium}$ Interaction

The  $\text{CH}_5^+ \cdots {}^4\text{He}$  interaction has been parameterized in terms of a NN-PES (NN-IP-CH5P-HE-2022-V0) using another automated procedure as described for the first time in Ref. 8, which is similar to the one used for fitting the molecular PES but deviating in crucial aspects as explained previously. The dataset used for this purpose is composed of 48000  $\text{CH}_5^+ \cdots {}^4\text{He}$  configurations. The RMSE associated with the training and validation set is 0.03 and 0.05 kJ/mol, respectively, and the quality of the fit is illustrated in Fig. S6. To further test this neural network description of

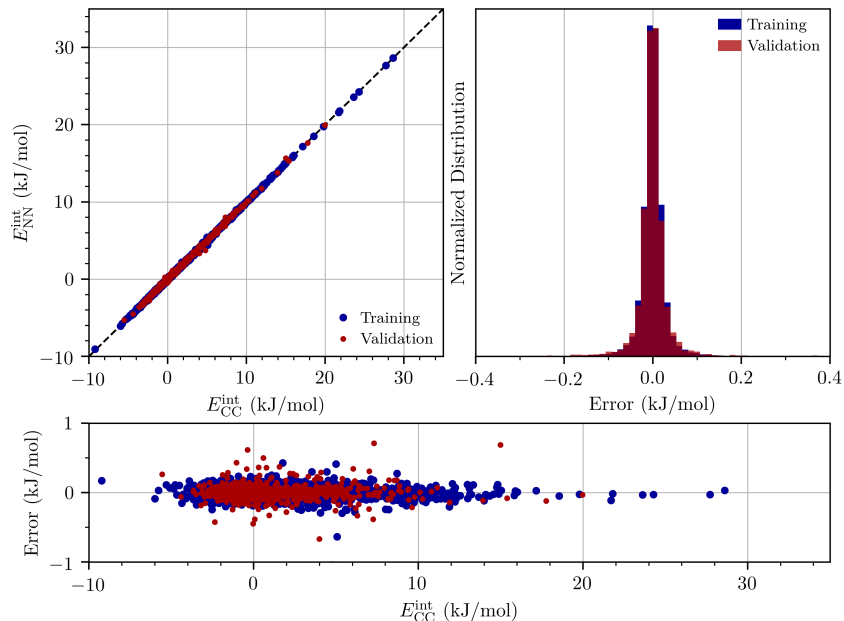


Figure S6. Analysis of the training of the  $\text{CH}_5^+ \cdots {}^4\text{He}$  NN-PES. Correlations of the interaction energies obtained by the NN-PES (NN) and the reference coupled cluster (CC) method (top left). Histogram (top right) and values (bottom) of the associated errors.

the  $\text{CH}_5^+ \cdots {}^4\text{He}$  interactions, we put it to a most stringent test by directly comparing the helium density (in terms of its spatial distribution function, SDF) obtained using the NN-PES and the CC reference method around a space-fixed molecular impurity. In practice, the interaction potential is first tabulated on a fine grid around the fixed molecule: For each point, the interaction energy is computed using both the NN-PES and the CC method. PIMC simulations of helium around the molecule are then performed using the precomputed energy value on the closest grid point. This allows us to compute approximate helium densities in Cartesian space around a fixed molecular impurity – even with the computationally expensive CC method. The results of this comparison are presented in Fig. S7 and clearly show that the NN-PES correctly reproduces the helium densities

around  $\text{CH}_5^+$  in all important configurations, namely e- $\text{C}_s$ , s- $\text{C}_s$  and  $\text{C}_{2v}$ , even for a large number of helium atoms (98 atoms here). Upon closer inspection, one can detect some small remaining differences for large numbers of  $^4\text{He}$  atoms (where smaller isovalues are required to visualize the larger clusters) around  $\text{CH}_5^+$  in the e- $\text{C}_s$  configuration; a similar observation has been made and analyzed earlier [8] in Figs. 3 and 4 therein. Nevertheless, the most prominent features of the density remain correctly described even for 98 helium atoms and the NN-PES, thus, still provides an accurate description of the helium density in these cases.

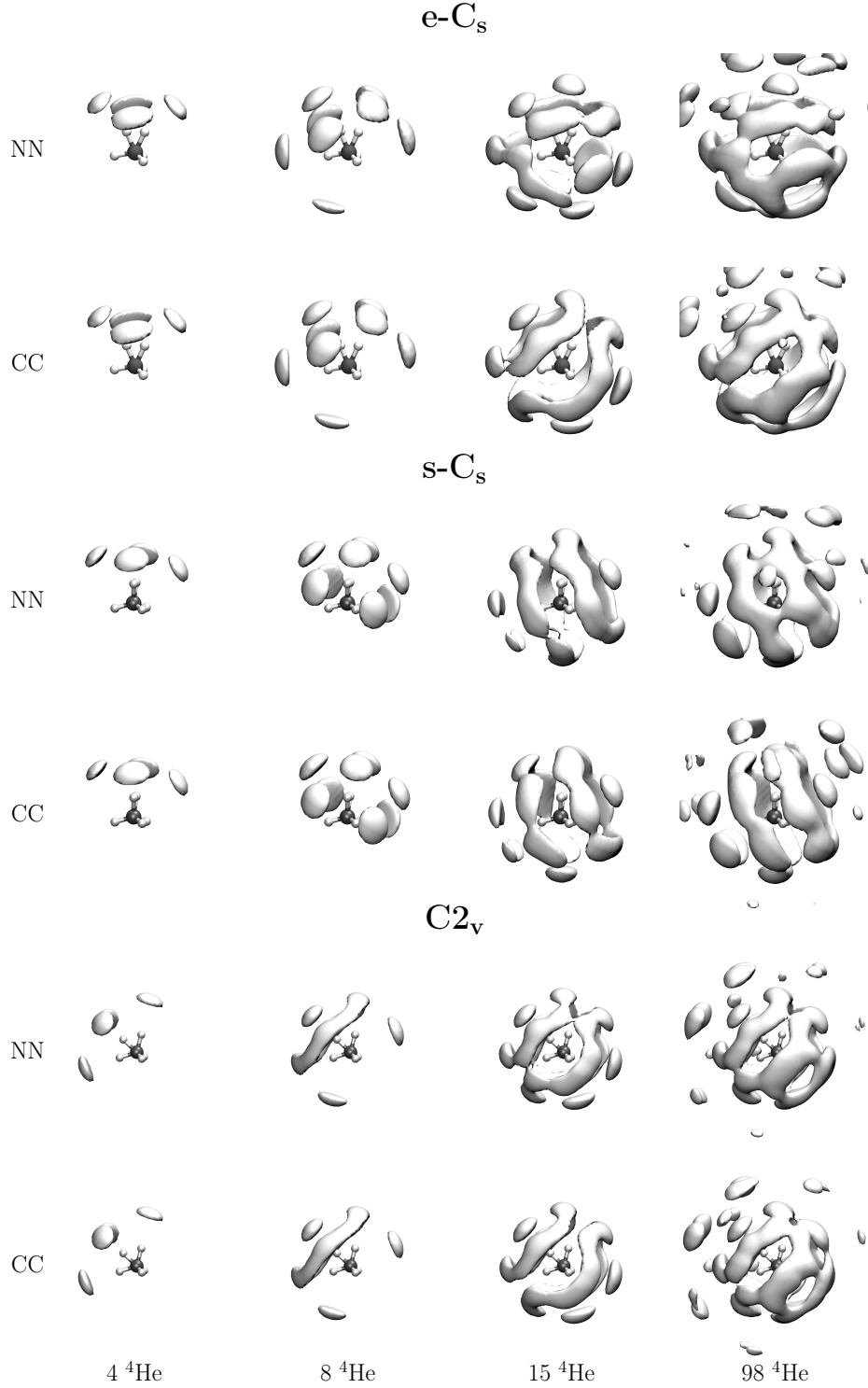


Figure S7. Helium densities (spatial distribution functions) around  $\text{CH}_5^+$  completely fixed in space in various representative configurations, e- $\text{C}_s$  (two first rows), s- $\text{C}_s$  (third and fourth rows) and  $\text{C}_{2v}$  (two last rows). The densities are computed by PIMC at  $T = 1.67\text{ K}$  without bosonic exchange and using potential energy values that have been precomputed with the NN-PES (NN) and the reference coupled cluster method (CC) on a fine grid around the fixed molecule. Isosurface values:  $0.035 N_{\text{He}}/\text{\AA}^3$  for 4 He,  $0.025 N_{\text{He}}/\text{\AA}^3$  for 8 He,  $0.020 N_{\text{He}}/\text{\AA}^3$  for 15 He and  $0.015 N_{\text{He}}/\text{\AA}^3$  for 98 He.



### E. $\text{CH}_4 \cdots \text{Helium}$ Interaction

As for  $\text{CH}_5^+ \cdots {}^4\text{He}$ , we use a dedicated high-dimensional NNP to describe the  $\text{CH}_4 \cdots {}^4\text{He}$  interaction potential (NN-IP-CH4-HE-2022-V0). The generation of the dataset as well as the training of the interaction potential are performed using the same automated approach as before. The dataset is composed of 47833  $\text{CH}_4 \cdots {}^4\text{He}$  configurations and the RMSE associated with the training and validation set is 0.004 and 0.005 kJ/mol, respectively. The quality of the fit is illustrated in Fig. S8, which clearly shows that the NN-PES is able to reproduce the CC reference to very high precision. To further test this description of the  $\text{CH}_4 \cdots {}^4\text{He}$  interaction, we put it to the same test as before and directly compare the helium densities obtained using the NN-PES and the CC reference method around a fixed molecular impurity in the minimum energy configuration. The results presented in Fig. S9 clearly show that this approach is again able to describe the helium solvation of the molecule with great accuracy since essentially no difference between the densities can be observed.

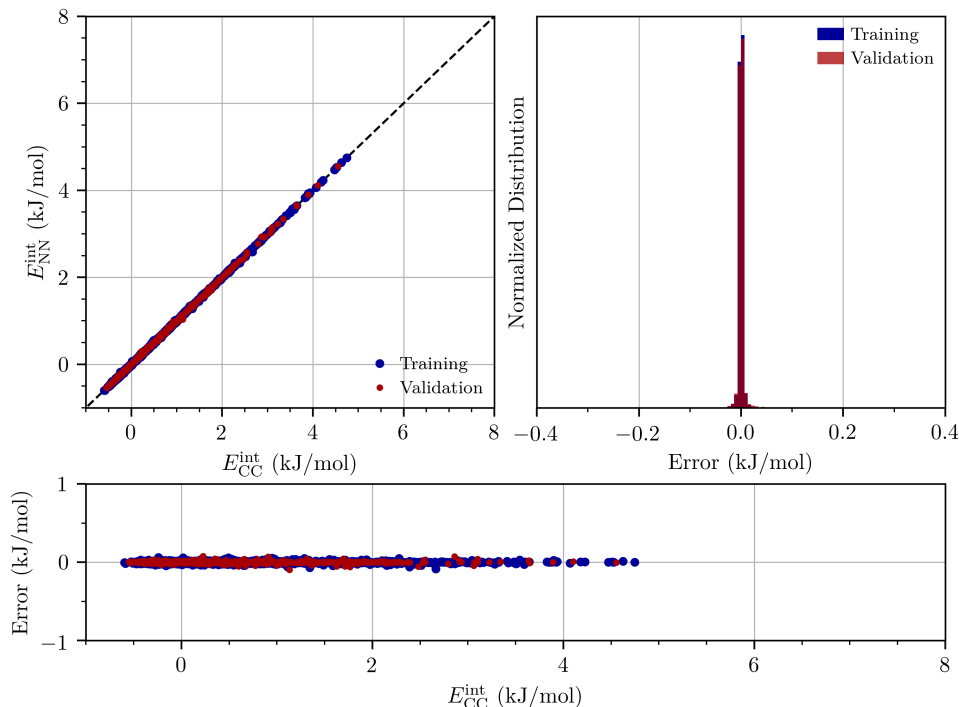


Figure S8. Analysis of the training of the  $\text{CH}_4 \cdots {}^4\text{He}$  NN-PES. Correlations of the interaction energies obtained by the NN-PES (NN) and the reference coupled cluster (CC) method (top left). Histogram (top right) and values (bottom) of the associated errors.

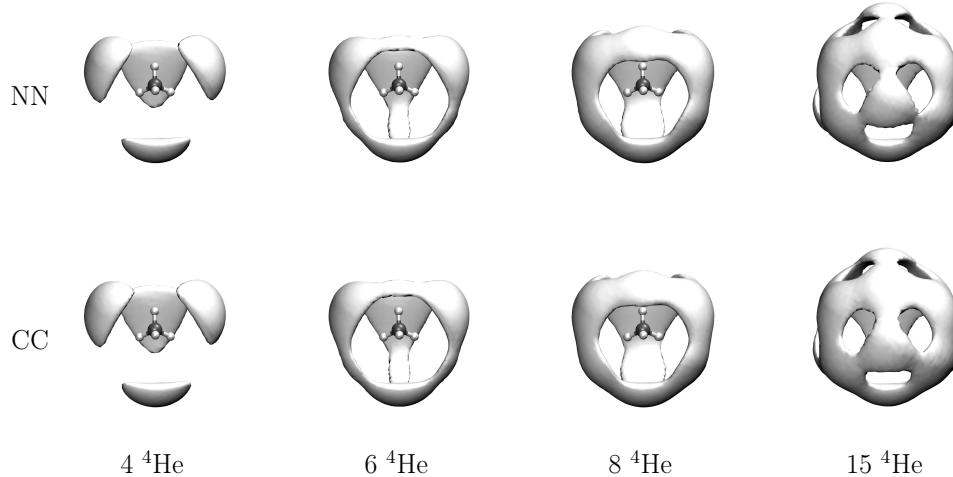


Figure S9. Helium densities (spatial distribution functions) around  $\text{CH}_4$  completely fixed in space in its minimum energy configuration. The densities are computed by PIMC at  $T = 1.67\text{K}$  without bosonic exchange and using potential energy values that have been precomputed with the NN-PES (NN) and the reference coupled cluster method (CC) on a fine grid around the fixed molecule. Isosurface values:  $0.0040 N_{\text{He}}/\text{\AA}^3$  for 4 and 6 He,  $0.0050 N_{\text{He}}/\text{\AA}^3$  for 8 He and  $0.0055 N_{\text{He}}/\text{\AA}^3$  for 15 He.

## II. SOLVATION SHELL STRUCTURE

In addition to the structural properties presented in the main text, we present here further details of the structure of the helium solvation shell. Various distributions are presented in Fig. S10, which show that helium around  $\text{CH}_5^+$  is much more structured than around  $\text{CH}_4$ , an effect that is the direct result of the much stronger interaction between helium and protonated methane as quantified in Fig. S11. One can also see from the distributions in Fig. S10 that completely neglecting the molecular degrees of freedom by fixing the two molecules at their minimum energy configurations does not qualitatively change the helium solvation shell structure for large clusters. In particular, in the large cluster limit,  $n = 60$ , the impact of molecular motion on the overall structure of the solvation shell is essentially negligible. Focusing more closely on the  $\text{C}\cdots\text{He}$  distance distributions, a clear shell structure appears around  $\text{CH}_5^+$  featuring a sharp first solvation shell localized between 2.5 and 4.8  $\text{\AA}$ , which is filled with 16  $^4\text{He}$  atoms as analyzed in detail in Fig. S12. In the case of  $\text{CH}_4$ , however, only a faint shell structure is observed with a first shell that is much less clearly defined and located between around 2.75 and 5.9  $\text{\AA}$ . Studying the evolution of the  $\text{C}\cdots\text{He}$  distance as a function of the number of helium atoms  $n$  in Fig. S12 shows that a second shell is formed around  $\text{CH}_5^+$  for  $n > 16$   $^4\text{He}$  atoms, see in particular the corresponding inset. The situation is, however, less clear around  $\text{CH}_4$  where a second shell can only be hinted for  $n > 20$   $^4\text{He}$  atoms. When looking

at the fraction of atoms that form the first shell it is evident that the second shell already starts to be gradually filled for  $n > 9$   $^4\text{He}$  atoms around  $\text{CH}_4$ , as seen in the inset of Fig. S12, whereas shell filling is sharp in the case of the strongly interacting  $\text{CH}_5^+$  molecule.

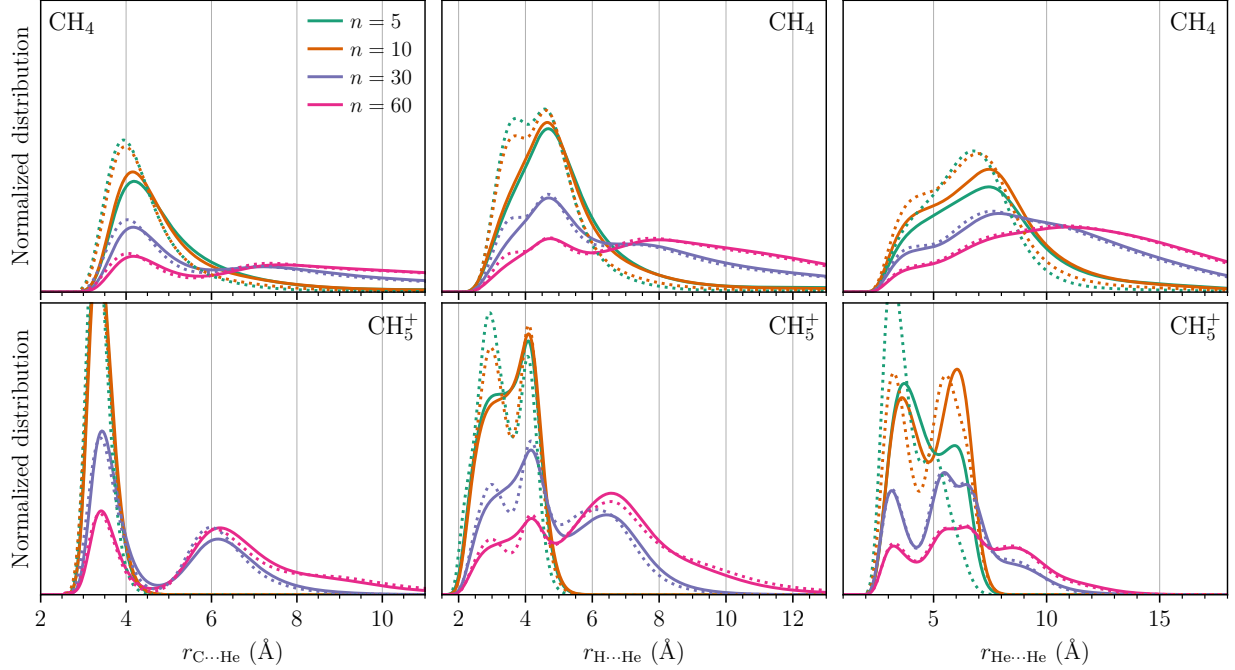


Figure S10. Structure of the helium solvation shell around  $\text{CH}_4$  (first row) and  $\text{CH}_5^+$  (second row) for different numbers  $n$  of  $^4\text{He}$  atoms at  $T = 0.5\text{ K}$ . The dotted lines correspond to molecules completely fixed in space in their minimum energy structures. The first column presents distributions of  $\text{C}\cdots\text{He}$  distances, the second column presents distributions of  $\text{H}\cdots\text{He}$  distances and the last column presents distributions of  $\text{He}\cdots\text{He}$  distances. All the distributions are normalized to unity.

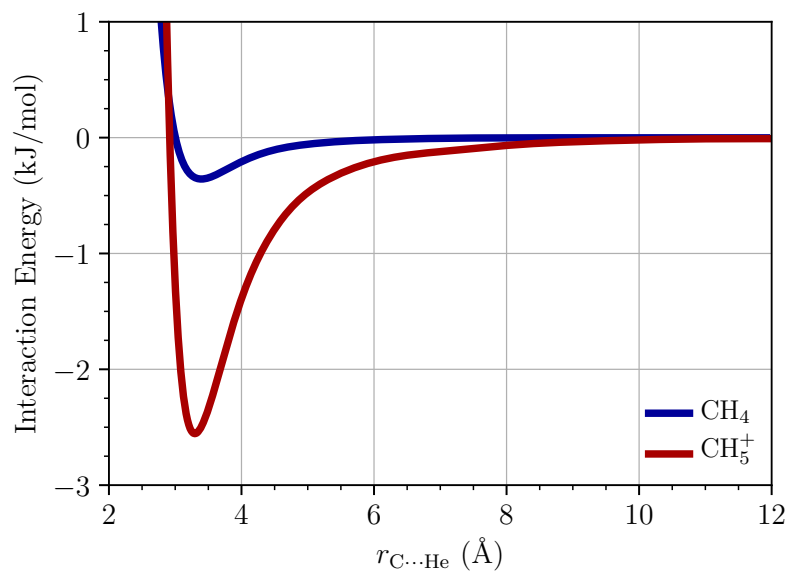


Figure S11. Interaction energy as a function of the  $\text{C}\cdots\text{He}$  distance along the direction of maximum interaction for both  $\text{CH}_4$  and  $\text{CH}_5^+$  fixed in their minimum energy structure.



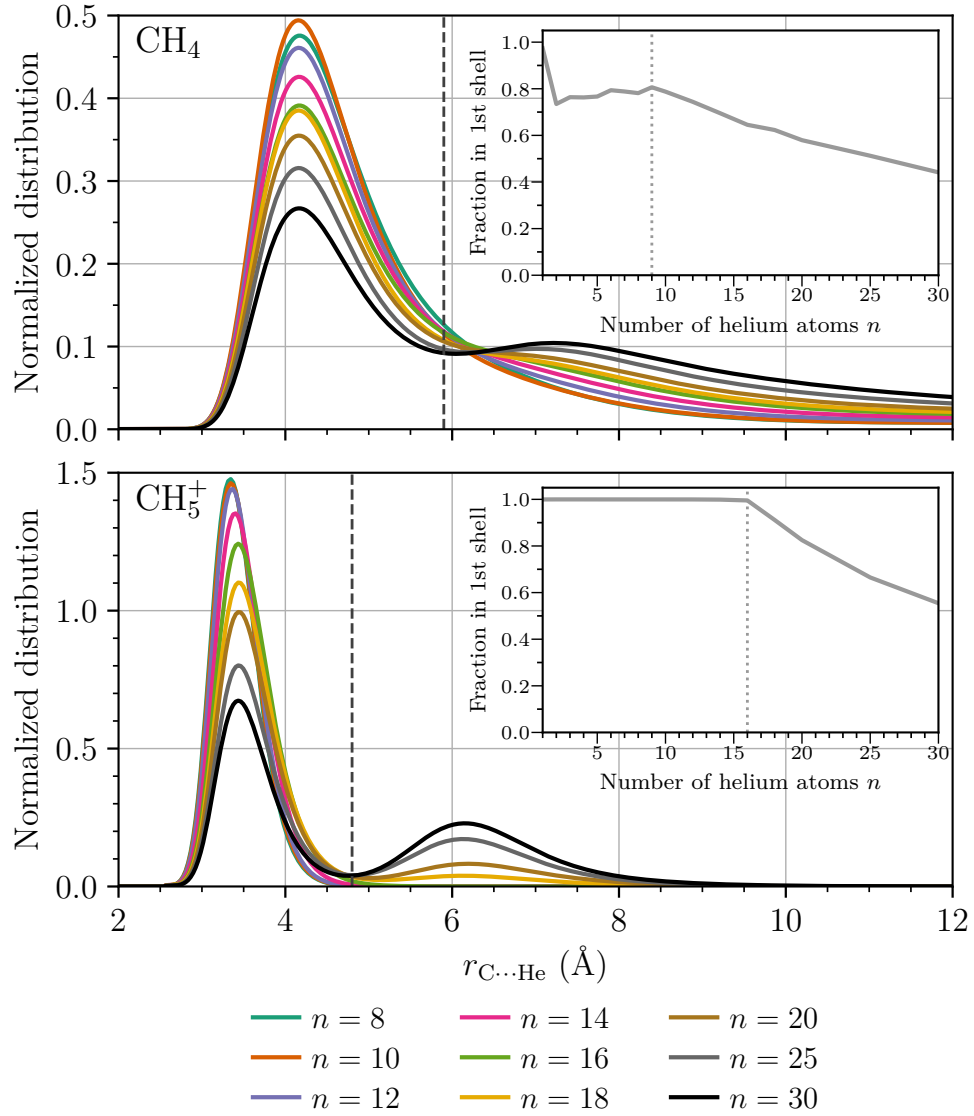


Figure S12. Distribution of C...He distances around  $\text{CH}_4$  (top) and  $\text{CH}_5^+$  (bottom) at  $T = 0.5$  K for different numbers of helium atoms  $n$  as provided below the plots. The insets show the fraction of helium atoms that are in the first shell as a function of the number of  $^4\text{He}$  atoms  $n$  computed by integrating the density in the first shell; the vertical dotted lines indicate the  $n$  values when the second shell starts to be gradually filled. The distance used to separate between first and second shell is 5.9 Å for  $\text{CH}_4$  and 4.8 Å for  $\text{CH}_5^+$  as marked by the dashed vertical lines in the main plots.

### III. SUPERFLUID ESTIMATORS

#### A. Superfluid Fraction

Within the two fluid model of superfluidity, the density of helium  $\rho$  is divided into a superfluid component  $\rho_s$  and a normal component  $\rho_n$  with

$$\rho = \rho_n + \rho_s. \quad (1)$$

The superfluid fraction can then be defined as the fraction of helium in the superfluid state  $f_s = \rho_s/\rho$  and is connected to the decrease of the effective moment of inertia  $I^{\text{eff}}$  that appears at temperatures lower than the critical temperature  $T_c$  of the superfluid transition

$$f_s = 1 - f_n = 1 - \frac{I^{\text{eff}}(T < T_c)}{I^{\text{eff}}(T = T_c)}, \quad (2)$$

with  $f_n = \rho_n/\rho$  being the normal fraction. This formula can of course only be used in cases where a proper superfluid phase transition appears for which a critical temperature can unambiguously be defined, as done experimentally for bulk  $^4\text{He}$  at ambient pressure (while assuming that the total density does not change as a function of temperature in that range). In this case,  $T_c = 2.17\text{ K}$  is the standard critical temperature of the lambda transition.

In the famous Andronikashvili experiment [16] the effective moment of inertia is measured through the angular frequency of a torsional oscillator immersed in liquid helium. Upon decreasing the temperature, the contribution of the helium to the total moment of inertia, i.e. the effective moment of inertia, decreases and reaches zero when the helium is entirely superfluid ( $f_s=1$ ). In simulations, the effective moment of inertia can be obtained using the following relation from linear response theory

$$I_\alpha^{\text{eff}} = \left. \frac{\partial \langle \hat{L}_\alpha \rangle}{\partial \omega} \right|_{\omega=0} \quad (3)$$

that connects the  $\alpha$  principal component of the effective moment of inertia to the response of helium to an infinitesimally slow rotation around the principal  $\vec{e}_\alpha$  axis; note that any axis can be taken in the homogeneous isotropic bulk limit. Within the path integral framework, Eq. (3) can be used to obtain the following expression for the effective moment of inertia

$$I_\alpha^{\text{eff}} = I_\alpha^{\text{cl}} - \frac{4m_{\text{He}}^2}{\beta \hbar^2} \langle A_\alpha^2 \rangle, \quad (4)$$

with  $I_\alpha^{\text{cl}}$  the  $\alpha$  principal component of the classical moment of inertia which can be expressed as

$$I_\alpha^{\text{cl}} = \left\langle \frac{m_{\text{He}}}{P} \sum_{i=1}^{N_{\text{He}}} \sum_{s=1}^P (\vec{e}_\alpha \times \vec{r}_{i,s}) \cdot (\vec{e}_\alpha \times \vec{r}_{i,s+1}) \right\rangle \quad (5)$$

and  $A_\alpha^2$  the square of the vectorial area of the Feynman paths

$$\vec{A} = \frac{1}{2} \sum_{i=1}^{N_{\text{He}}} \sum_{s=1}^P \vec{r}_{i,s} \times \vec{r}_{i,s+1}, \quad (6)$$

i.e. the area spanned by the ring polymer, projected along the  $\vec{e}_\alpha$  direction. The second term on the right hand side of equation (4) quantifies the quantum reduction of the effective moment of inertia due to superfluidity. The superfluid fraction is thus obtained in a similar way as in equation (2)

$$f_s^\alpha = 1 - \frac{I_\alpha^{\text{eff}}}{I_\alpha^{\text{cl}}} = \frac{4m_{\text{He}}^2 \langle A_\alpha^2 \rangle}{\beta \hbar^2 I_\alpha^{\text{cl}}}. \quad (7)$$

This estimator is referred to as the “area estimator” and has been first introduced for the study of pure helium clusters [17]; a detailed discussion and derivation can be found in Ref. 18.

Obviously, superfluidity is a macroscopic phenomenon and the concept is not well defined for finite size systems. Nevertheless, it has been demonstrated that clusters of pure helium as small as 64  $^4\text{He}$  atoms exhibits clear “manifestations of superfluid behavior” [17]. Moreover, the study of rotational constants of various molecules as a function of the number  $n$  of helium atoms has revealed the onset of superfluid behavior for doped clusters composed of less than 10  $^4\text{He}$  atoms, leading to many studies on the concept of “microscopic molecular superfluid response” [18–21].

It is important to note that the area estimator, which has been devised for sufficiently large clusters, will necessarily overestimate the superfluid fraction for small clusters, since also non-exchanging paths span a finite area. In particular, in the limit of only one helium atom Eq. (7) leads to an unphysical finite superfluid fraction and for small clusters it can result in  $f_s$  values that are systematically too large and even greater than unity. The estimator is formally only valid in the thermodynamic limit for which the long exchange paths completely dominate the contributions due to the smaller non-exchanging paths. Thus, Eq. (7) should be used with great caution for very small clusters. In order to circumvent this problem, a rescaled estimator, that aims at removing the contribution of non exchanging paths from the area estimator, has recently been introduced [18, 22]. This so-called “exchange estimator” is defined as

$$f_s^\alpha = \frac{I_{\alpha,\text{MB}}^{\text{eff}} - I_{\alpha,\text{BE}}^{\text{eff}}}{I_{\alpha,\text{MB}}^{\text{eff}}} = 1 - \frac{I_{\alpha,\text{BE}}^{\text{eff}}}{I_{\alpha,\text{MB}}^{\text{eff}}} \quad (8)$$

with  $I_{\text{MB}}^{\text{eff}}$  the effective moment of inertia, obtained from a path integral simulation in which the helium follows Maxwell-Boltzmann statistics (i.e. without quantum exchange and thus neglecting the bosonic nature of  $^4\text{He}$ ) and  $I_{\text{BE}}^{\text{eff}}$  is the effective moment of inertia obtained from a bosonic treatment of the helium. This estimator is able to isolate the contribution to the area coming only from the exchanging paths and has thus been dubbed the “exchange” (X) estimator.

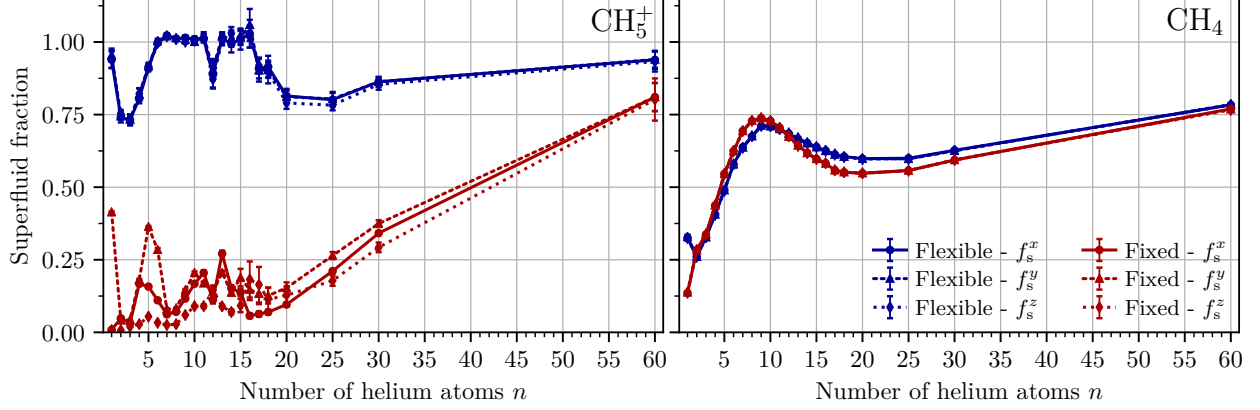


Figure S13. Superfluid fraction along the  $x, y$  and  $z$  direction at  $T = 0.5$  K as a function of the number of helium atoms around  $\text{CH}_5^+$  (left) and  $\text{CH}_4$  (right) computed using the area estimator (Eq. (7)). The red lines corresponds to the results obtained with a molecule completely fixed in its minimum energy configuration, while the blue lines show the results obtained with a fully flexible impurity.

Fig. S13 shows the superfluid fraction obtained using the standard area estimator as a function of the number of helium atoms computed in the space fixed frame (or laboratory frame). The first observation is the striking difference between the superfluid fractions obtained around a fully flexible and a completely fixed  $\text{CH}_5^+$ , discussed in detail in the main text of the manuscript. Neglecting the molecular degrees of freedom of  $\text{CH}_5^+$  results in a significant suppression of the superfluid fraction. As discussed in detail in the main manuscript, this effect directly comes from the high degree of localization of  $^4\text{He}$  in the first shell that hinders the creation of long exchange cycles and thus suppresses superfluidity in the first shell. Upon increasing the size of the cluster, the difference between the flexible and fixed case is considerably reduced – but only since the relative impact of what happens in the first shell on the total superfluid fraction of the entire cluster decreases for large  $n$  values. The effect remains, however, present in the first shell as can be seen from the local superfluid density (Fig. S16 and Fig. 4 of the main text) for  $\text{CH}_5^+ \cdot \text{He}_{60}$ . In the case of  $\text{CH}_4$ , this impact of the molecular degrees of freedom is not found and the values of  $f_s$  obtained with a flexible or fixed impurity are very similar. It is interesting to note as well that around the fixed  $\text{CH}_5^+$  molecule the obtained superfluid fraction is not isotropic due to the pronounced asymmetry of the  $\text{CH}_5^+ \cdots \text{He}$  potential, thus yielding different values  $f_s^\alpha$  for the three different directions  $\alpha$ . This effect is not present in the flexible case due to molecular rotations and is also not seen around the fixed  $\text{CH}_4$  molecule due to the high symmetry of the  $\text{CH}_4 \cdots \text{He}$  potential.

For very small numbers of helium atoms, significant superfluid fractions are obtained around the flexible  $\text{CH}_5^+$  and, in particular, a finite superfluid fraction is observed with a single helium

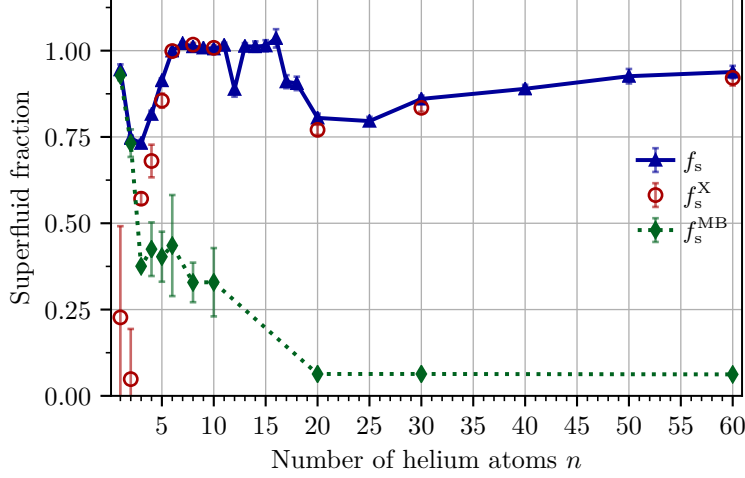


Figure S14. Superfluid fraction  $f_s$  computed using the area estimator (Eq. (7)) and  $f_s^X$  computed using the exchange estimator (Eq. (8)) as a function of the number of helium atoms around flexible  $\text{CH}_5^+$  at  $T = 0.5$  K. The superfluid fraction is computed as an average over the three directions since  $f_s$  is isotropic here. Additionally the superfluid fraction formally computed using the area estimator applied to non-bosonic Maxwell-Boltzmann simulations,  $f_s^{MB}$ , is included as well to give an estimation of the contribution of the non-exchanging paths to  $f_s$  obtained from the area estimator.

atom, which is a clear illustration of the failure of the area estimator for very small clusters as is well-known from the literature. Upon increasing the number of helium atoms  $n$  for  $\text{CH}_5^+$ , the superfluid fraction quickly reaches unity for  $6 < n < 16$  except for the special case of 12  $^4\text{He}$  atoms, discussed in detail in the following. For  $n > 16$ , the total superfluid fraction in the entire cluster drops due to the creation of the second helium solvation shell, which features a smaller density that prevents the creation of long exchange paths. Upon building this second solvation shell, the associated density increases again for  $n \gg 16$  and so does that the superfluid fraction reaching around 0.9 for the largest cluster of 60  $^4\text{He}$  atoms. In the case of  $\text{CH}_4$ , the superfluid fraction reaches a first maximum for  $n = 9$ , which also corresponds to the beginning of the building of a second solvation shell (see Fig. S12), in which the density and thus the superfluid fraction is lower. Upon building this second solvation shell, the superfluid fraction increases again to reach a value of around 0.75 for the largest cluster of 60  $^4\text{He}$  atoms.

In order to estimate the validity of the superfluid fractions computed here using the area estimator, we have performed additional simulations without bosonic exchange for a few selected numbers of helium atoms around flexible protonated methane in order to compute the superfluid fraction using the exchange estimator [18, 22] of Eq. (8). The comparison between the superfluid fraction obtained using the two estimators is presented in Fig. S14. It is clear that except for very

small numbers of helium atoms, the area estimator provides a very good estimation of the superfluid fraction, since both estimators provide almost the same value for  $n > 5$   $^4\text{He}$  atoms (thus the blue triangles and red circles are close to each other). Only in the small cluster limit (in particular for  $\leq 4$ ), the exchange estimator (red circles) yields substantially smaller  $f_s$  values and eventually approaches the expected limit, namely zero, within error bars.

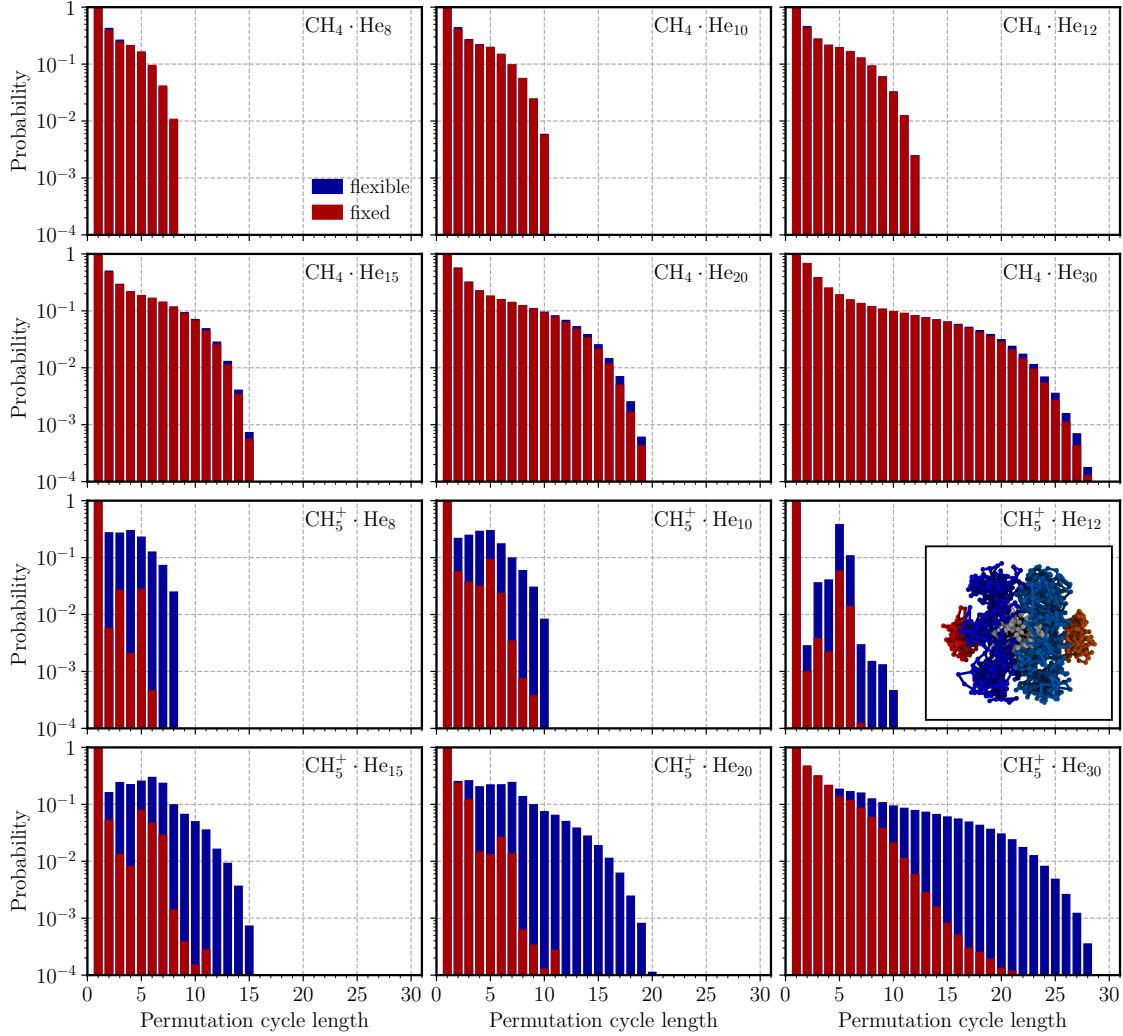


Figure S15. Probability of finding at least one exchange path of specific length for  $\text{CH}_4 \cdot {}^4\text{He}_n$  (first two rows) and  $\text{CH}_5^+ \cdot {}^4\text{He}_n$  (second two rows) at  $T = 0.5$  K for different clusters sizes  $n$  as indicated. Data for the flexible and fixed impurities are shown in blue and red, respectively; note that blue is superimposed by red where not visible. The inset of  $\text{CH}_5^+ \cdot {}^4\text{He}_{12}$  depicts a representative snapshot from the simulation illustrating a typical arrangement of the helium atoms for this very special case, see text. The helium beads represented with the same color belongs to the same exchange cycle.

It is well-known that superfluidity is directly connected to the presence of long exchange cy-

cles [23–25], i.e. of path lengths comparable to the system size, and the statistics of exchange path length, as shown in Fig. S15, can thus provide complementary insight into the origin of the superfluid response. The exchange path statistics clearly confirm that, in the case of  $\text{CH}_4$ , the molecular degrees of freedom have no significant impact on bosonic exchange and thus on the superfluid behavior of helium. In the case of  $\text{CH}_5^+$  however, there is a clear coupling between the molecular motion and bosonic exchange and, in particular, neglecting the molecular degrees of freedom by fixing  $\text{CH}_5^+$  in space tends to significantly reduce the probability of building long exchange cycles, which reduces the superfluid response.

A special case appears for  $\text{CH}_5^+ \cdot \text{He}_{12}$ , for which a sudden drop of the superfluid fraction is also noticed in Fig. S13. This effect is related to a particularly stable configuration of the helium atoms, forming two parallel rings of five atoms around  $\text{CH}_5^+$  with the last two atoms being located at two opposite ends of the molecule, as shown in the inset of  $\text{CH}_5^+ \cdot {}^4\text{He}_{12}$  in Fig. S15. This configuration in Cartesian space leads to a special distribution in permutation space as well, with the exchange path length of five being overrepresented, as such rings are mostly found in exchange cycles involving all five atoms. Similar configurations have been previously observed for instance in para- $\text{H}_2$  clusters doped with a water molecule [26], thus indicating that this specific topology of the exchange path might be a universal feature of doped bosonic clusters featuring a strong molecule...solvent interaction.

## B. Local Superfluid Density

The well-known connection between the presence of long exchange paths and superfluidity [23–25] can actually be used as a proxy to obtain local information on the superfluid behavior of the helium solvent. In particular, an estimator of the local superfluid density  $\rho_s(r)$  was introduced [25] based on the distributions of helium atoms involved in an exchange path longer than a certain cutoff length  $l$ ,

$$\rho_s^{(l)}(\vec{r}) = \sum_{p>l}^{N_{\text{He}}} \rho_p(\vec{r}) \quad , \quad (9)$$

where  $\rho_p(\vec{r})$  is the local density of helium involved in an exchange cycle of length  $p$  at point  $\vec{r}$  in space. Figure S16 displays the local superfluid density obtained using this “local exchange path estimator” for different  $l$  parameters where  $r$  is the distance between the carbon nucleus in  $\text{CH}_5^+$  and  $\text{CH}_4$  with respect to helium. In particular, the impact of the choice of the cutoff to distinguish between “short” and “long” exchange path is investigated in the following. While the



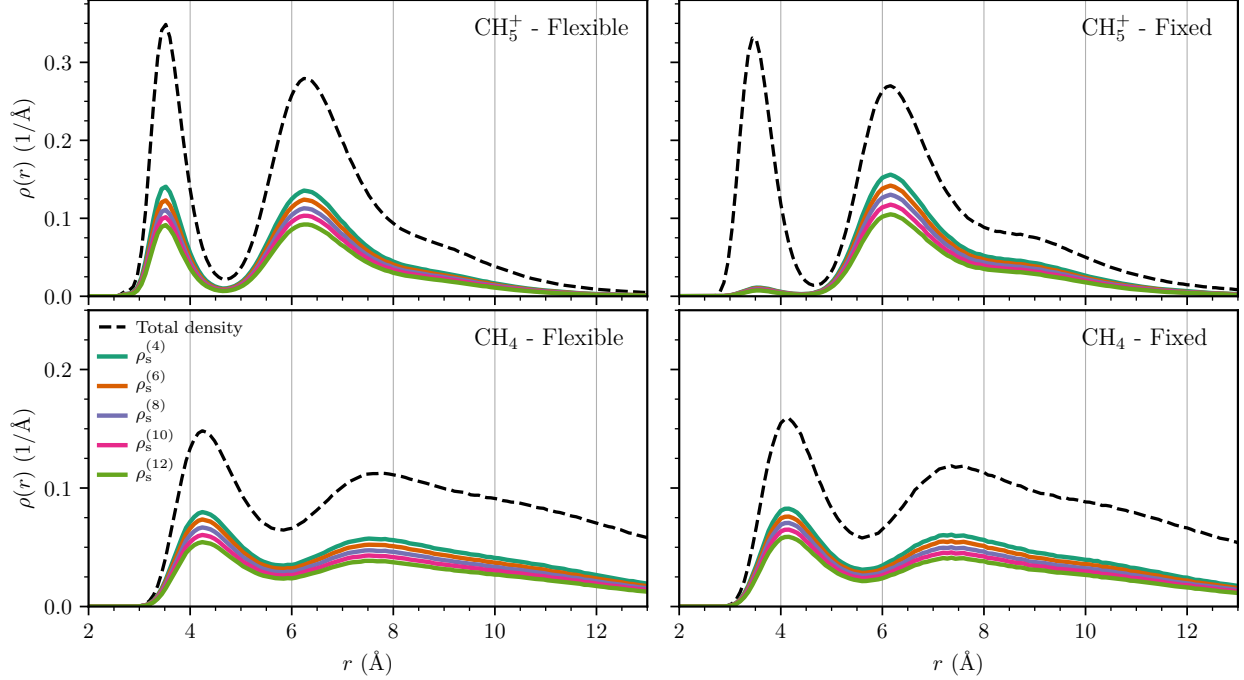


Figure S16. Local superfluid density  $\rho_s^{(l)}$  for  $\text{CH}_5^+ \cdot \text{He}_{60}$  (first row)  $\text{CH}_4 \cdot \text{He}_{60}$  (second row) computed using the “local exchange path estimator” of Eq. (9) at  $T = 0.5 \text{ K}$  using different values of the cutoff length  $l$  where  $r$  is the distance between the carbon nucleus with respect to helium, see text. Left and right columns are for flexible and fixed molecules, respectively.

obtained superfluid densities clearly depend on the value of the cutoff parameter  $l$ , their shapes remain unchanged for different values of  $l$  and Eq. (9) thus provides a relatively robust estimator of the superfluid density. The results presented in the main manuscript are obtained using a cutoff of  $l = 6$ . However, the estimator tends to systematically underestimate the superfluid density, as expected based on its definition. Short paths, and in particular non-exchanging ones, strongly contribute to the normal density in this estimator, even though such paths are also present in a fully superfluid case. Nevertheless, this estimator of the local superfluid density still grants access to a well-defined locally resolved estimation of the superfluid response as we will demonstrate in what follows by comparing the results provided by this estimator (as discussed in the main manuscript) with those using another local estimator.

An alternative local estimator based on the area of the Feynman paths in a similar way as the (global) area estimator of the superfluid fraction has also been developed [27, 28]. In particular, a “local area estimator” of the superfluid density has been introduced, which leads to the correct

value of the effective moment of inertia [28]

$$I_{\alpha}^{\text{eff}} = \int (\rho(\vec{r}) - \rho_s^{\alpha}(\vec{r})) r_{\perp}^2 d^3\vec{r} \quad (10)$$

$$I_{\alpha}^{\text{eff}} = I_{\alpha}^{\text{cl}} - \int \rho_s^{\alpha}(\vec{r}) r_{\perp}^2 d^3\vec{r}. \quad (11)$$

The last term in the right hand side clearly represents the quantum reduction of the effective moment inertia due to superfluidity and is given by

$$\int \rho_s^{\alpha}(\vec{r}) r_{\perp}^2 d^3\vec{r} = \frac{4m_{\text{He}}^2}{\beta\hbar^2} \langle A_{\alpha}^2 \rangle, \quad (12)$$

from which the following superfluid density estimator can be obtained [28]

$$\rho_s^{\alpha}(\vec{r}) = \frac{4m_{\text{He}}^2 \langle A_{\alpha} A_{\alpha}(\vec{r}) \rangle}{\beta\hbar^2 r_{\perp}^2}, \quad (13)$$

with  $A_{\alpha}(\vec{r})$  the local contribution to the area defined as

$$A_{\alpha}(\vec{r}) = \frac{1}{2} \sum_{i=1}^{N_{\text{He}}} \sum_{s=1}^P (\vec{r}_{i,s} \times \vec{r}_{i,s+1})_{\alpha} \delta(\vec{r}_{i,s} - \vec{r}). \quad (14)$$

A local superfluid fraction can then be defined as well,

$$\frac{\rho_s^{\alpha}(\vec{r})}{\rho(\vec{r})} = \frac{4m_{\text{He}}^2 \langle A_{\alpha} A_{\alpha}(\vec{r}) \rangle}{\beta\hbar^2 I^{\text{cl}}(\vec{r})}, \quad (15)$$

which can be used to compute the values of superfluid fraction associated with different regions, such as the first and second shell, by locally averaging the contribution to the local exchange area and moment of inertia [28]. This can be used furthermore to define a radial superfluid fraction or equivalently a radial superfluid density,

$$\rho_s^{\alpha}(r) = \frac{4m_{\text{He}}^2 \langle A_{\alpha} A_{\alpha}(r) \rangle}{\beta\hbar^2 I^{\text{cl}}(r)} \rho(r) \quad (16)$$

as shown in the bottom panel of Fig. 4 of the main text. Note that the distance  $r$  corresponds here to the distance of helium with respect to the center of mass of the molecule computed using all the beads (rather than to the C atom of the respective molecule as used in Fig. S16). The differences between the total helium density in Fig. 4 of the main text are simply due to this change of the reference point for computing distances, noting that the center of mass distance is a more natural choice for the local area estimator. Indeed, the vectorial product in Eq. (14) requires a common origin for the two position vectors, which should thus not depend on the bead index and we chose here to use the molecular center of mass computed using all the beads.

As mentioned in the main text, both estimators provide the same overall picture for both impurities, in particular the distance modulations of the superfluid response within the first and

second helium shells when comparing the flexible to the fixed impurity scenario. Yet, despite providing such qualitative agreement, the local area estimator leads to superfluid densities that are typically quantitatively different in numbers from the ones obtained using the “local exchange path estimator” (see Fig. S16). In particular, with this estimator, we find that the global superfluid fraction associated with the  $\text{CH}_4\cdot\text{He}_{60}$  complex is 0.86 which is larger in number than the value of 0.78 obtained using the associated global superfluid fraction estimator of Eq. (7). In the case of the  $\text{CH}_5^+\cdot\text{He}_{60}$  complex, the obtained superfluid density indicates that the cluster is essentially fully superfluid around flexible  $\text{CH}_5^+$  with an associated global superfluid fraction of 0.96, which is indeed very similar to the value of 0.94 that we obtained using the global estimator of Eq. (7). In particular, the first solvation shell is fully superfluid. In the case of the fixed protonated methane, the obtained superfluid density indicates, as expected, a much lower superfluid fraction estimated to be around 0.68 which is even smaller than the value of 0.78 obtained with the global estimator. The superfluid density in the first shell is particularly impacted and the associated superfluid fraction dropped to 0.28 as a result of the strong localization of helium as discussed in the main manuscript.

In summary, both estimators fully consistently disclose that sufficiently large  $\text{CH}_5^+\cdot\text{He}_n$  complexes feature a strong superfluid response of the first (frozen) solvation shell in the fully flexible case, and thus manifestations of supersolid behavior, which is lost if the large-amplitude rovibrational degrees of freedom of the molecule are neglected by fixing all intramolecular molecular degrees of freedom, as discussed in detail in the main manuscript. Recall that this phenomenon, which can only be observed with sufficiently many helium atoms to fully solvate the molecular impurity, thus filling the first solvation shell, cannot appear in the microsolvation limit and is thus strikingly different from what has been discovered earlier [29] for very small  $\text{CH}_5^+\cdot\text{He}_n$  up to  $n = 4$ .

### C. Microsolvation Limit

The microsolvation of  $\text{CH}_5^+$  up to a maximum number of four helium atoms has been studied some time back [29, 30] which we discuss in the following in relation to our current work that focuses on novel effects of this impurity seen in the realm of large  $^4\text{He}$  clusters. Previously, an intricate coupling between the molecular motion of the impurity and bosonic exchange of helium has been discovered for such tiny  $\text{CH}_5^+\cdot^4\text{He}_n$  clusters with  $n$  up to four helium atoms [29]. Such small system sizes  $n$  are of particular interest to  $^4\text{He}$ -based tagging spectroscopy [31–33]. Given the lack of a well-defined, unique estimator to compute the superfluid fraction in the limit of a small

number of  $^4\text{He}$  atoms (as discussed here in Sec. III A), which is particularly relevant for  $\text{CH}_5^+ \cdot ^4\text{He}_n$  with  $n \leq 4$ , the previous analysis [29] has been performed entirely at the qualitative level. In particular, the exchange path statistics of those paths that include all available  $n$   $^4\text{He}$  atoms, i.e. as few as  $n = 2, 3$  and  $4$  in this case, has been studied; this approach closely follows pioneering work [24, 25] on using “sufficiently long” exchange cycles as a proxy to detect superfluid behavior.

Here, in stark contrast, we are interested in the opposite limit to microsolvation, namely completely filling the first solvation shell and going beyond by studying large clusters with up to  $n = 60$   $^4\text{He}$  atoms that solvate the  $\text{CH}_5^+$  molecule. We demonstrate based on Fig. S14 that the area and exchange estimators reviewed in Sec. III A provide very similar superfluid fractions only for  $n \geq 6$  which remains so all the way up to the largest cluster  $n = 60$ . We therefore refrain here from discussing the superfluid fraction for  $\text{CH}_5^+ \cdot ^4\text{He}_n$  clusters with  $n < 6$  given the strongly different  $f_s$  results and, thus, ambiguity in the microsolvation limit. Moreover, we study here only either the fully flexible or the frozen  $\text{CH}_5^+$  core within the  $\text{CH}_5^+ \cdot ^4\text{He}_n$  clusters, whereas major insights on the impact of large-amplitude motion on bosonic exchange within microsolvated clusters with  $n \leq 4$  were enabled in the previous study [29] by performing so-called “e- $\text{C}_s$  restrained simulations” to generate data on a useful reference system (namely the one that allows only for small-amplitude motion while not being fixed in space). This aspect is not at all in the focus of the present investigation on  $\text{CH}_5^+ \cdot ^4\text{He}_n$  clusters that is devoted to what happens in the limit of large clusters, in particular beyond having filled the first solvation shell. For this purpose, we introduce  $\text{CH}_4 \cdot ^4\text{He}_n$  clusters to provide the proper reference system to assess effects due to large-amplitude motion (which only operate in  $\text{CH}_5^+$ ) since  $\text{CH}_4$  is a standard quasi-rigid molecule subject to small-amplitude motion that is well described by quasi-harmonic deviations from a unique equilibrium structure.

Apart from that, we achieved major improvements of the accuracy of the interactions, i.e. the  $\text{CH}_5^+$  potential energy surface and the  $\text{CH}_5^+ \cdots ^4\text{He}$  interaction potential that we can now use compared to previously [29]. In that previous work, a simple force field description of the  $\text{CH}_5^+$  potential energy surface has been used, the so-called POSflex model [34], where all five C–H bond distances have the same equilibrium length, thus all protons move on a sphere centered around the carbon site. This force field is computationally highly efficient, but only allows for a merely qualitatively satisfactory description of the properties of  $\text{CH}_5^+$  as demonstrated previously [34], since POSflex does not take into account the characteristically different lengths [15] of the three-center versus two-center C–H bonds within  $\text{CH}_5^+$ . Secondly, the potential constructed previously to describe the  $\text{CH}_5^+ \cdots ^4\text{He}$  interactions is based on a complicated, traditional force field-like representation fitted against coupled cluster interaction energies [35]. Unfortunately, this potential is only able to

provide a satisfactory description of very small  $\text{CH}_5^+ \cdot {}^4\text{He}_n$  clusters up to only four  ${}^4\text{He}$  atoms [35], whereas it has been found to fail even qualitatively for  $n > 4$ . Thus, the present study would not have been possible using this existing interaction potential.

In the current work, in stark contrast to our previous investigation [29], we greatly improved the quality of all interactions, both intra- and intermolecular, and pushed them to the converged coupled cluster level, CCSD(T), enabled by using our high-dimensional neural network potential approach for finite systems [8, 9] at what is often called “chemical accuracy”. This major development is comprehensively presented in a self-contained manner in Sec. I where we describe in detail the generation and validation of the  $\text{CH}_5^+$  and  $\text{CH}_4$  potential energy surfaces as well as the  $\text{CH}_5^+ \cdots {}^4\text{He}$  and  $\text{CH}_4 \cdots {}^4\text{He}$  interaction potentials that we introduced and used in the present investigation for the first time.

Another significant improvement of the present study versus our previous work [29] is related to the colored-noise thermostating scheme within the path integral approach to effectively enhance the convergence of the Trotter decomposition. The currently used PIQTB technique [36], carefully validated for use at very low temperatures [37], allows us to reach a temperature of 0.5 K in a path integral molecular dynamics setup, whereas previously, using the PIGLET technique [38, 39], we were able to reach only 1.25 K, where bosonic exchange effects are of course much less pronounced.

Overall, our present quantum simulation approach significantly transcends, both in accuracy and convergence, the one used a few years back [29] to study microsolvated  $\text{CH}_5^+ \cdot {}^4\text{He}_n$  clusters with  $n \leq 4$  in many ways. Only these significant improvements grant access to accurately simulating large  $\text{CH}_5^+ \cdot {}^4\text{He}_n$  clusters – which provides the basis to discover a novel effect, namely *manifestations of supersolid behavior*. We refer the interested reader to a recent review where all these major improvement of our neural network-based bosonic path integral simulation methodology, which enables converged quantum simulations of complex molecular systems such as the present one at very low temperatures, are explained and validated in detail [40].

- 
- [1] J. Behler and M. Parrinello, Generalized Neural-Network Representation of High-Dimensional Potential-Energy Surfaces, *Phys. Rev. Lett.* **98**, 146401 (2007).
  - [2] J. Behler, First Principles Neural Network Potentials for Reactive Simulations of Large Molecular and Condensed Systems, *Angew. Chem. Int. Ed.* **56**, 12828 (2017).
  - [3] R. A. Kendall, T. H. Dunning, and R. J. Harrison, Electron affinities of the first-row atoms revisited. Systematic basis sets and wave functions, *J. Chem. Phys.* **96**, 6796 (1992).
  - [4] D. E. Woon and T. H. Dunning, Gaussian basis sets for use in correlated molecular calculations. IV. Calculation of static electrical response properties, *J. Chem. Phys.* **100**, 2975 (1994).
  - [5] T. B. Adler, G. Knizia, and H.-J. Werner, A simple and efficient CCSD(T)-F12 approximation, *J. Chem. Phys.* **127**, 221106 (2007).
  - [6] G. Knizia, T. B. Adler, and H.-J. Werner, Simplified ccscd(t)-f12 methods: Theory and benchmarks, *J. Chem. Phys.* **130**, 054104 (2009).
  - [7] H.-J. Werner, P. J. Knowles, G. Knizia, F. R. Manby, and M. Schütz, Molpro: a general-purpose quantum chemistry program package, *WIREs Comput Mol Sci* **2**, 242 (2012).
  - [8] C. Schran, F. Uhl, J. Behler, and D. Marx, High-dimensional neural network potentials for solvation: The case of protonated water clusters in helium, *J. Chem. Phys.* **148**, 102310 (2017).
  - [9] C. Schran, J. Behler, and D. Marx, Automated Fitting of Neural Network Potentials at Coupled Cluster Accuracy: Protonated Water Clusters as Testing Ground, *J. Chem. Theory Comput.* **16**, 88 (2020).
  - [10] J. Behler, RuNNer: A program for constructing high-dimensional neural network potentials; Georg-August-Universität Göttingen, Germany, <https://www.uni-goettingen.de/de/560580.html>.
  - [11] M. Gastegger and P. Marquetand, High-Dimensional Neural Network Potentials for Organic Reactions and an Improved Training Algorithm, *J. Chem. Theory Comput.* **11**, 2187 (2015).
  - [12] J. Behler, Atom-centered symmetry functions for constructing high-dimensional neural network potentials, *J. Chem. Phys.* **134**, 074106 (2011).
  - [13] S. F. Boys and F. Bernardi, The calculation of small molecular interactions by the differences of separate total energies. Some procedures with reduced errors, *Mol. Phys.* **19**, 553 (1970).
  - [14] O. Marchetti and H.-J. Werner, Accurate calculations of intermolecular interaction energies using explicitly correlated coupled cluster wave functions and a dispersion-weighted mp2 method, *J. Phys. Chem. A* **113**, 11580 (2009).
  - [15] D. Marx and M. Parrinello, Structural quantum effects and three-centre two-electron bonding in  $\text{CH}_5^+$ , *Nature* **375**, 216 (1995).
  - [16] E. L. Andronikashvili, *J. Phys. USSR* **10**, 201 (1946).
  - [17] P. Sindzingre, M. L. Klein, and D. M. Ceperley, Path-integral Monte Carlo study of low-temperature  $^4\text{He}$  clusters, *Phys. Rev. Lett.* **63**, 1601 (1989).
  - [18] T. Zeng and P.-N. Roy, Microscopic molecular superfluid response: theory and simulations, *Rep. Prog.*

- Phys. **77**, 046601 (2014).
- [19] J. Tang, Y. Xu, A. R. W. McKellar, and W. Jäger, Quantum Solvation of Carbonyl Sulfide with Helium Atoms, *Science* **297**, 2030 (2002).
  - [20] J. Tang, A. R. W. McKellar, F. Mezzacapo, and S. Moroni, Bridging the Gap between Small Clusters and Nanodroplets: Spectroscopic Study and Computer Simulation of Carbon Dioxide Solvated with Helium Atoms, *Phys. Rev. Lett.* **92**, 145503 (2004).
  - [21] A. R. W. McKellar, Y. Xu, and W. Jäger, Spectroscopic Exploration of Atomic Scale Superfluidity in Doped Helium Nanoclusters, *Phys. Rev. Lett.* **97**, 183401 (2006).
  - [22] T. Zeng, G. Guillon, J. T. Cantin, and P.-N. Roy, Probing the Superfluid Response of para-Hydrogen with a Sulfur Dioxide Dopant, *J. Phys. Chem. Lett.* **4**, 2391 (2013).
  - [23] D. M. Ceperley, Path integrals in the theory of condensed helium, *Rev. Mod. Phys.* **67**, 279 (1995).
  - [24] W. Krauth, Quantum Monte Carlo Calculations for a Large Number of Bosons in a Harmonic Trap, *Phys. Rev. Lett.* **77**, 3695 (1996).
  - [25] Y. Kwon and K. B. Whaley, Atomic-Scale Quantum Solvation Structure in Superfluid Helium-4 Clusters, *Phys. Rev. Lett.* **83**, 4108 (1999).
  - [26] T. Zeng, H. Li, and P.-N. Roy, Simulating Asymmetric Top Impurities in Superfluid Clusters: A para-Water Dopant in para-Hydrogen, *J. Phys. Chem. Lett.* **4**, 18 (2013).
  - [27] E. W. Draeger and D. M. Ceperley, Superfluidity in a Doped Helium Droplet, *Phys. Rev. Lett.* **90**, 065301 (2003).
  - [28] Y. Kwon, F. Paesani, and K. B. Whaley, Local superfluidity in inhomogeneous quantum fluids, *Phys. Rev. B* **74**, 174522 (2006).
  - [29] F. Uhl and D. Marx, Quantum Microsolvation of Protonated Methane with  $^4\text{He}$ : Large-Amplitude Motion Heavily Influences Bosonic Exchange, *Phys. Rev. Lett.* **123**, 123002 (2019).
  - [30] F. Uhl and D. Marx, Helium Tagging of Protonated Methane in Messenger Spectroscopy: Does It Interfere with the Fluxionality of  $\text{CH}_5^+$ ?, *Angew. Chem. Int. Ed.* **57**, 14792 (2018).
  - [31] J. Roithová, A. Gray, E. Andris, J. Jašík, and D. Gerlich, Helium tagging infrared photodissociation spectroscopy of reactive ions, *Acc. Chem. Res.* **49**, 223 (2016).
  - [32] M. Töpfer, T. Salomon, H. Kohguchi, O. Dopfer, K. M. T. Yamada, S. Schlemmer, and O. Asvany, Double Resonance Rotational Spectroscopy of Weakly Bound Ionic Complexes: The Case of Floppy  $\text{CH}_3^+-\text{He}$ , *Phys. Rev. Lett.* **121**, 143001 (2018).
  - [33] O. Asvany, S. Schlemmer, T. Szidarovszky, and A. G. Császár, Infrared Signatures of the  $\text{HHe}_n^+$  and  $\text{DHe}_n^+$  ( $n = 3-6$ ) Complexes, *J. Phys. Chem. Lett.* **10**, 5325 (2019), <https://doi.org/10.1021/acs.jpcllett.9b01911>.
  - [34] F. Uhl, L. Walewski, H. Forbert, and D. Marx, Adding flexibility to the “particles-on-a-sphere” model for large-amplitude motion: POSflex force field for protonated methane, *J. Chem. Phys.* **141**, 104110 (2014).
  - [35] D. Kuchenbecker, F. Uhl, H. Forbert, G. Jansen, and D. Marx, Constructing accurate interaction



- potentials to describe the microsolvation of protonated methane by helium atoms, *Phys. Chem. Chem. Phys.* **19**, 8307 (2017).
- [36] F. Briec, H. Dammak, and M. Hayoun, Quantum Thermal Bath for Path Integral Molecular Dynamics Simulation, *J. Chem. Theory Comput.* **12**, 1351 (2016).
- [37] C. Schran, F. Briec, and D. Marx, Converged Colored Noise Path Integral Molecular Dynamics Study of the Zundel Cation down to Ultralow Temperatures at Coupled Cluster Accuracy, *J. Chem. Theory Comput.* **14**, 5068 (2018).
- [38] M. Ceriotti and D. E. Manolopoulos, Efficient First-Principles Calculation of the Quantum Kinetic Energy and Momentum Distribution of Nuclei, *Phys. Rev. Lett.* **109**, 100604 (2012).
- [39] F. Uhl, D. Marx, and M. Ceriotti, Accelerated path integral methods for atomistic simulations at ultra-low temperatures, *J. Chem. Phys.* **145**, 054101 (2016).
- [40] F. Briec, C. Schran, F. Uhl, H. Forbert, and D. Marx, Converged quantum simulations of reactive solutes in superfluid helium: The Bochum perspective, *J. Chem. Phys.* **152**, 210901 (2020).